von Hagke, C., Cederbom, C. E., Oncken, O., Stoeckli, D. F., Rahn, M. K., Schlunegger, F. (2012): Linking the northern Alps with their foreland: The latest exhumation history resolved by low-temperature thermochronology. - Tectonics, 31, TC5010

DOI: 10.1029/2011TC003078

Linking the northern Alps with their foreland: The latest exhumation history resolved by low-temperature thermochronology

C. von Hagke,[1,2] C. E. Cederbom,[3] O. Oncken,[1] D. F. Stöckli,[4] M. K. Rahn,[5] and F. Schlunegger[6]

Received 1 December 2011; revised 27 August 2012; accepted 15 September 2012; published 23 October 2012.

[1] The evolution of the Central Alpine deformation front (Subalpine Molasse) and its undeformed foreland is recently debated because of their role for deciphering the late orogenic evolution of the Alps. Its latest exhumation history is poorly understood due to the lack of late Miocene to Pliocene sediments. We constrain the late Miocene to Pliocene history of this transitional zone with apatite fission track and (U-Th)/He data. We used laser ablation inductively coupled mass spectrometry for apatite fission track dating and compare this method with previously published and unpublished external detector method fission track data. Two investigated sections across tectonic slices show that the Subalpine Molasse was tectonically active after the onset of folding of the Jura Mountains. This is much younger than hitherto assumed. Thrusting occurred at 10, 8, 6–5 Ma and potentially thereafter. This is contemporaneous with reported exhumation of the External Crystalline Massifs in the central Alps. The Jura Mountains and the Subalpine Molasse used the same detachments as the External Crystalline Massifs and are therefore kinematically coupled. Estimates on the amount of shortening and thrust displacement corroborate this idea. We argue that the tectonic signal is related to active shortening during the late stage of orogenesis.

Citation: von Hagke, C., C. E. Cederbom, O. Oncken, D. F. Stöckli, M. K. Rahn, and F. Schlunegger (2012), Linking the northern Alps with their foreland: The latest exhumation history resolved by low-temperature thermochronology, *Tectonics*, *31*, TC5010, doi:10.1029/2011TC003078.

1. Introduction

[2] Recently, numerous studies have tried to unveil the late Neogene exhumation history of the central Alps [e.g., *Schlunegger and Simpson*, 2002; *Willett et al.*, 2006; *Reinecker et al.*, 2008; *Rosenberg and Berger*, 2009; *Vernon et al.*, 2009; *Glotzbach et al.*, 2010; *Valla et al.*, 2012; *Weisenberger et al.*, 2012] and their adjacent northern foreland, the Molasse Basin [e.g., *Cederbom et al.*, 2004; *Willett and Schlunegger*, 2010; *Cederbom et al.*, 2011; *Schlunegger and Mosar*, 2011]. These studies show that kilomdeter-scale erosion occurred within these regions, but it remains unclear whether this is a consequence of climate-induced post-orogenic isostatic rebound [e.g., *Cederbom et al.*, 2004; *Champagnac et al.*, 2009; *Cederbom et al.*, 2011], active shortening during the late stages of orogenesis [e.g., *Persaud and Pfiffner*, 2004; *Reinecker et al.*, 2008] or regional uplift in response to mantle processes [e.g., *Cederbom et al.*, 2011]. One of the key reasons for this ambiguity is the lack of high-resolution information on spatial resolution of active deformation at the orogenic front and its foreland basin. In this paper, our aim is to contribute to this debate by quantifying the timing and magnitude of shortening across the Subalpine Molasse, which forms the southern, folded and thrusted part of the foreland basin and is as such a key element, linking the Alps with their foredeep [*Vollmayr and Wendt*, 1987].

[3] In the central Alps, the External Crystalline Massifs, in particular, the Aar and Gotthard Massifs, are kinematically linked with the foreland [e.g., *Pfiffner*, 1986; *Pfiffner et al.*, 1990]. While differing in detail, most authors report low-temperature thermochronology data that corroborate Neogene uplift of these massifs. *Reinecker et al.* [2008], *Michalski and Soom* [1990] and *Weisenberger et al.* [2012] report constant exhumation of ~0.5 km/Myr at the northern flank of the Aar Massif since 10 Ma. *Vernon et al.* [2009] and *Glotzbach et al.* [2010] report a phase of accelerated exhumation of

[1]Department of Lithosphere Dynamics, Helmholtz Centre Potsdam, GFZ German Research Centre for Geosciences, Potsdam, Germany.
[2]Now at Division of Geological and Planetary Sciences, California Institute of Technology, Pasadena, California, USA.
[3]Department of Land Use Planning and Climate Adaptation, Swedish Geotechnical Institute, Linköping, Sweden.
[4]Jackson School of Geosciences, University of Texas at Austin, Austin, Texas, USA.
[5]Swiss Federal Nuclear Safety Inspectorate, Brugg, Switzerland.
[6]Institute of Geological Sciences, University of Bern, Bern, Switzerland.

Corresponding author: C. von Hagke, Division of Geological and Planetary Sciences, California Institute of Technology, MC 100-23, Pasadena, CA 91125, USA. (vonhagke@caltech.edu)

0278-7407/12/2011TC003078

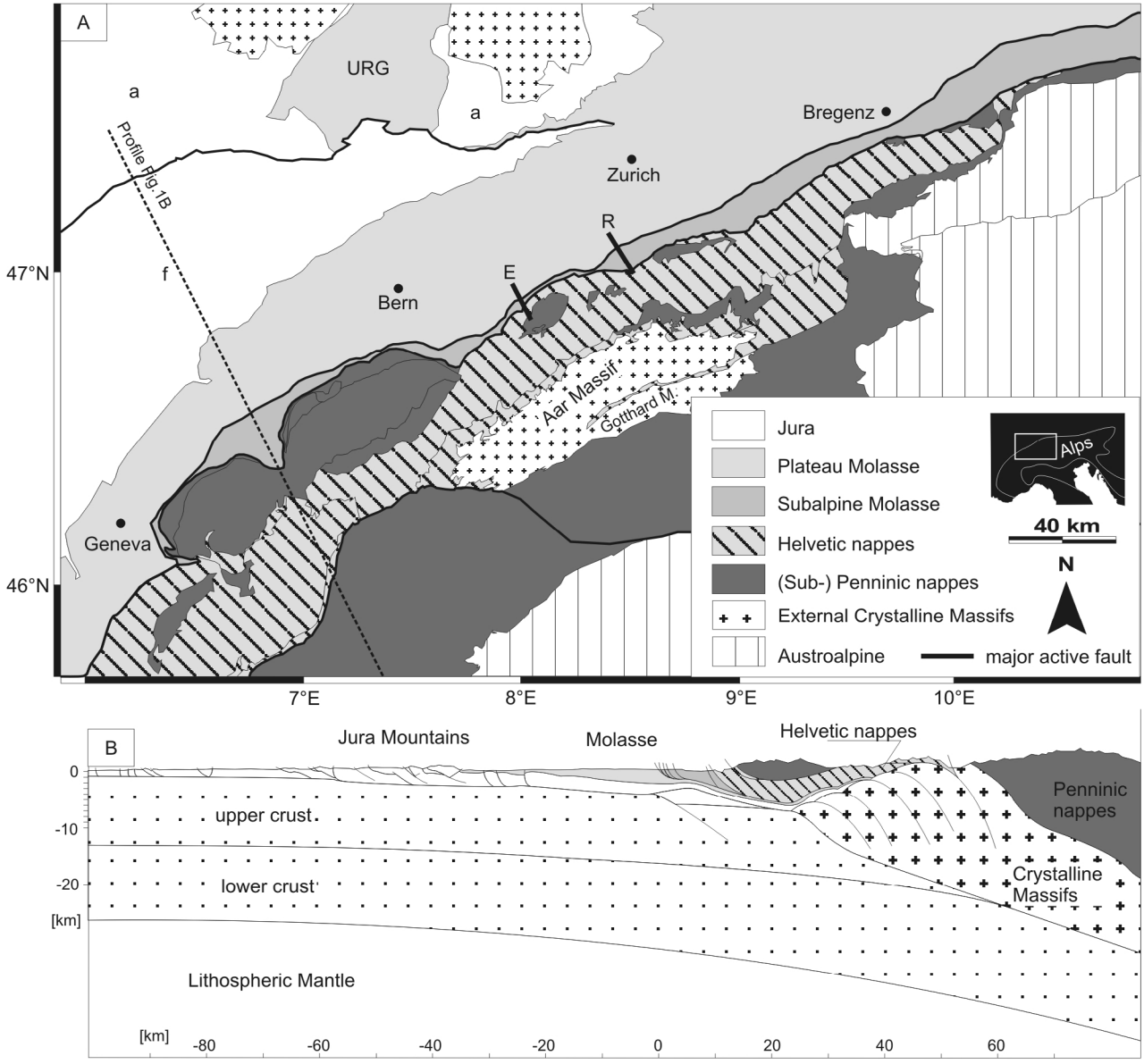

Figure 1. (a) Tectonic map of the northern central Alps and the adjacent foreland based on the work by *Spicher* [1980]. URG, Upper Rhine Graben; f, folded Jura; a, autochthonous Jura; E, trace of Entlebuch profile; and R, trace of Rigi profile indicated by black line. (b) Profile across the Alps modified after *Burkhard and Sommaruga* [1998].

~0.7 km/Myr for the Aar and Gotthard Massif between circa 10 and 7 Ma and subsequent exhumation at a rate of 0.5 km/Myr. *Valla et al.* [2012] report even higher rates of 2–4 km/Myr for the time span of 8–10 Ma followed by rates of 0.3–0.5 km/Myr until present.

[4] In contrast to the External Crystalline Massifs, the late Neogene exhumation history of the foreland is less constrained. This is mostly due to the lack of preserved sediments spanning the time interval between the late Miocene and the Pliocene, which were removed by erosion [*Schegg et al.*, 1997; *Kuhlemann and Kempf*, 2002; *Cederbom et al.*, 2004; *Mazurek et al.*, 2006; *Cederbom et al.*, 2011; *Schlunegger and Mosar*, 2011]. It is commonly inferred that thrusting in the proximal part of the basin, the so-called Subalpine Molasse, ceased with the onset of folding of the more external Jura Mountains, which started after 12 Ma, possibly as late as 9 Ma [*Laubscher*, 1992; *Bollinger et al.*, 1993; *Burkhard and Sommaruga*, 1998; *Becker*, 2000] (Figure 1). An increase in erosion rate since 5 Ma has been postulated [*Kuhlemann*, 2000]. Also, apatite fission track (AFT) data from boreholes [*Cederbom et al.*, 2004, 2011] indicate rapid erosion starting at 5 Ma, or possibly at 10 Ma [*Mazurek et al.*, 2006], which the authors attributed to a combination of climatic, tectonic, and geodynamic causes. This event is roughly coincident with the cessation of thin-skinned thrusting [*Laubscher*, 1961, 1992; *Sommaruga*, 1997, 1999; *Affolter and Gratier*, 2004] and onset of erosion in the Jura Mountains [*Ustaszewski and Schmid*, 2006; *Willett and Schlunegger*, 2010]. Recent tectonic activity within the Jura Mountains related to deep, intrabasement

detachment underneath the basin has been suggested by *Mosar* [1999] based on exhumation and seismicity data and *Becker* [2000] based on in situ stress measurements. In agreement with that, *Ustaszewski et al.* [2005], *Giamboni et al.* [2004], and *Ustaszewski and Schmid* [2006, 2007] found a late Pliocene change from thin- to thick-skinned tectonics at the northern fringe of the Jura fold and thrust belt at low strain rates. Finally, *Madritsch et al.* [2010] recorded largely aseismic recent deformation of the Mesozoic cover of the Jura Mountains and seismogenic faulting within the underlying basement. These partly contrasting interpretations of a link between deformation of the Jura, the External Crystalline Massifs and the Subalpine Molasse are mainly based on a lack of high-resolution exhumation data from the proximal basin border.

[5] Here we explore the kinematic evolution of the Subalpine Molasse that forms the Central Alpine deformation front at high resolution. To this end, we analyze vertical and horizontal sections for patterns of low-temperature thermochronometric ages and discuss them together with previously published data sets. We sampled two sections across the border between the Helvetic thrust nappes, the Subalpine Molasse and the flat-lying Plateau Molasse at a high spatial resolution, particularly in both the hanging and footwall of faults in order to bracket the age when these faults were active. We particularly combine AFT and apatite (U-Th-Sm)/He analyses to better constrain the timing, rate and style of exhumation in the Subalpine Molasse.

2. Regional Geologic Context

2.1. General Introduction

[6] The North Alpine Foreland Basin extends ~700 km from Haute Savoie (France) in the west through Switzerland and Bavaria to Vienna (Austria) in the east. It is a classic peripheral foreland basin whose stratigraphy, structure and formation have been studied for more than a hundred years [e.g., *Äppli*, 1897; *Heim*, 1919; *Cadisch*, 1928] and for which many geodynamic concepts have been tested [e.g., *Ganss and Schmidt-Thomé*, 1953; *Trümpy*, 1980; *Homewood et al.*, 1986; *Pfiffner*, 1986; *Schlunegger et al.*, 1997; *Sinclair*, 1997b; a; *Sissingh*, 1997; *Kuhlemann and Kempf*, 2002; *Pfiffner et al.*, 2002; *Berger et al.*, 2005b, 2005a].

[7] The formation of the basin is attributed to progressive flexural bending of the downgoing European Plate adjacent to the approaching rising Alps in Miocene time [*Pfiffner*, 1986; *Sinclair et al.*, 1991; *Burkhard and Sommaruga*, 1998; *Pfiffner et al.*, 2002; *Schlunegger et al.*, 2007]. Consequently, the northern boundary of the wedge-shaped basin propagated into the foreland through time, while the southernmost (and oldest) deposits were continuously incorporated into the Alpine orogen [*Homewood et al.*, 1986; *Sinclair and Allen*, 1992]. Together with the Jura fold and thrust belt the Molasse Basin forms the most external part of the Alpine chain [*Burkhard*, 1990] (Figure 1).

[8] Starting in the Paleogene, the collision history of the Alps was dominated by the foreland-directed propagation of the Alpine front across the southern European plate margin [*Homewood et al.*, 1986; *Pfiffner*, 1986; *Burkhard*, 1990; *Sinclair and Allen*, 1992; *Burkhard and Sommaruga*, 1998; *Delacou et al.*, 2004]. However, the outward propagation of deformation is not uniform and single-staged along the strike of the orogen. In the Western Swiss Molasse, deformation shifted from a proximal position in the Subalpine Molasse across most of the basin to the more distal Jura Mountains (Figure 2). This is in contrast to the Eastern Alps, where distal deformation remained fixed along the Subalpine Molasse. Some have argued that thrusting in the Western Swiss Molasse basin ceased at circa 12 Ma in conjunction with the jump to Jura thrusting [*Burkhard and Sommaruga*, 1998]. In the Jura Mountains, deformation proceeded until at least late Pliocene time [*Liniger*, 1964; *Bollinger et al.*, 1993; *Kälin*, 1997; *Mosar*, 1999; *Ustaszewski and Schmid*, 2007]. It appears to continue at very slow rates today involving the basement blocks in thick-skinned deformation [*Mosar*, 1999; *Giamboni et al.*, 2004; *Ustaszewski et al.*, 2005; *Ustaszewski and Schmid*, 2007; *Madritsch et al.*, 2008; *Madritsch et al.*, 2010].

2.2. Tertiary Basin Evolution

[9] Sedimentation in the Molasse Basin started in Paleocene-Eocene time with deposition of flysch that continued until late Eocene to early Oligocene times [*Matter et al.*, 1980; *Homewood et al.*, 1986; *Allen et al.*, 1991; *Lihou and Allen*, 1996; *Ruffini et al.*, 1997; *Sinclair*, 1997a; 1997b; *Kempf and Pfiffner*, 2004]. This was followed by at least two major regressive cycles from marine to freshwater deposits [*Matter et al.*, 1980]. Deposition of Molasse sediments prograded northward between the early Oligocene and the late Miocene. Accumulation of Molasse deposits probably continued until the Pliocene, when the Molasse Basin was uplifted and eroded [*Cederbom et al.*, 2004; *Mazurek et al.*, 2006; *Cederbom et al.*, 2011].

[10] The Swiss Molasse stratigraphic sequence is subdivided into four lithostratigraphic units (Figure 2): the Lower Marine Molasse (UMM) and the Lower Freshwater Molasse (USM), which together form the first regressive cycle. It is followed by the Upper Marine Molasse (OMM) and the Upper Freshwater Molasse (OSM), both of which are of Miocene age and comprise the second regressive cycle. By convention, the German abbreviations are used for these different lithostratigraphic units [*Matter et al.*, 1980]. For a more detailed description of the stratigraphy of the Swiss Molasse Basin, the reader is referred to *Matter et al.* [1980] and *Schlunegger* [1999].

[11] A sub-Quaternary unconformity truncates the Molasse deposits because of extensive erosion during the Pliocene, as revealed by vitrinite reflectance and previously published AFT studies in the Swiss part of the basin [*Schegg*, 1992; *Schegg et al.*, 1997; *Schegg and Leu*, 1998; *Cederbom et al.*, 2004; *Mazurek et al.*, 2006; *Cederbom et al.*, 2011]. Hence, the complete stratigraphic record of the foreland basin covers the time range from early Tertiary (including the Flysch units at the base of the foreland sequence) to 11.5 Ma [*Rahn and Selbekk*, 2007]. The timing of the end of deposition, the timing of onset of erosion and the amount of removed section remain speculative [*Schlunegger and Mosar*, 2011]. Remnants of younger deposits at the distal edge of the basin are preserved only in synclines of the Jura [*Kälin*, 1997].

[12] The morphology of the basin was overprinted by several periods of glacial erosion, which led to strong valley deepening at the Alpine margin at circa 0.8 Ma [*Haeuselmann et al.*, 2007; *Valla et al.*, 2011]. Today, rivers draining the Alps cut into clastic sediments of the Last Glacial Maximum.

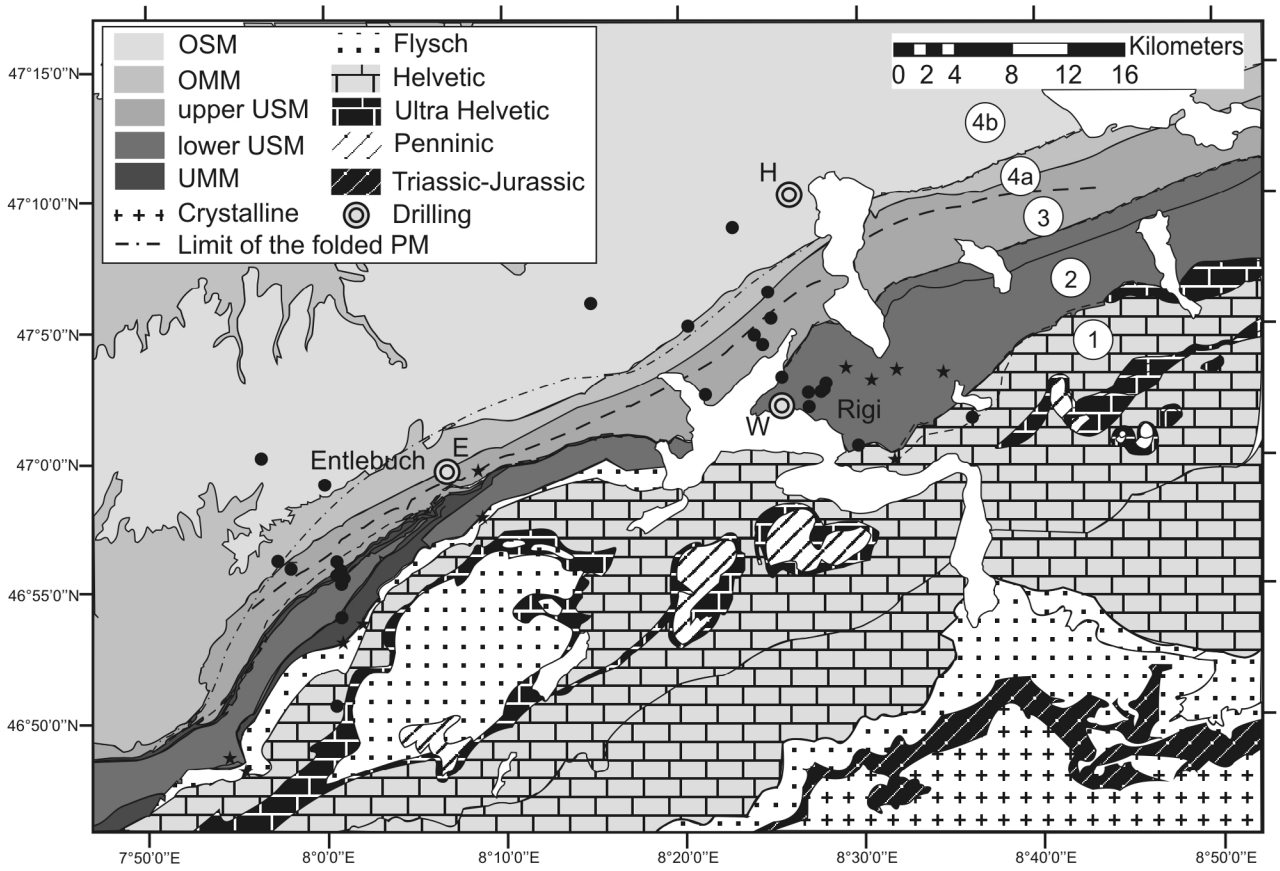

Figure 2. Detailed geological map of the study area. Black dots denote sampling localities for apatite fission track and (U-Th-Sm)/He data analyzed by C. von Hagke, black stars denote sample points of apatite fission track data analyzed by M. Rahn (partly published by *Cederbom et al.* [2004]). Four tectonic slices (1–4) are indicated as discussed in the text. TS-4a represents the folded and tilted part of the Plateau Molasse, TS-4b represents the northern flat lying part. Drillings discussed in the text are E (Entlebuch-1), W (Weggis-1) and H (Hünenberg-1). OSM, Upper Freshwater Molasse; OMM, Upper Marine Molasse; USM, Lower Freshwater Molasse; UMM, Lower Marine Molasse; PM, Plateau Molasse.

2.3. The Subalpine Molasse

[13] The Subalpine Molasse comprises an imbricate stack of proximal foreland basin deposits north of the basal alpine thrust. These were accreted into the Alpine wedge in early Miocene times [*Schlunegger et al.*, 1997; *Kempf et al.*, 1999]. During the Miocene, a triangle zone developed in parts of the basin, separating the Subalpine Molasse from the weakly deformed to flat-lying Plateau Molasse [*Vollmayr and Wendt*, 1987]. The structure of the triangle zone is constrained by borehole and seismic data [*Müller et al.*, 1988; *Berge and Veal*, 2005].

[14] Because the southern limits of the basin are hidden beneath tectonically higher units, it is difficult to restore the original basin width. Unfolding the Subalpine Molasse yields total shortening of at least 10 km, but could be as large as 50 km [*Burkhard and Sommaruga*, 1998]. For the eastern Swiss Molasse basin, *Kempf et al.* [1999] estimated a total of 28 km of shortening.

[15] We present an overview map including all sample sites (Figure 2), two detailed maps for the two sample transects across the Rigi and Entlebuch areas (Figure 3) and two corresponding detailed cross sections (Figures 4 and 5). The Rigi cross section has only minor modifications with respect to a balanced cross section published by *Burkhard* [1990]. The Entlebuch cross section, which is located ~30 km farther west, represents a new reconstruction of the tectonic architecture and is mainly based on previous work by *Trümpy* [1980], *Burkhard* [1990], *Pfiffner* [2010], and on our own mapping. It considers the data from the borehole Entlebuch-1, which were projected into the cross section [*Vollmayr and Wendt*, 1987]. This well is situated ~10 km east of the sample profile. Both cross sections cover all relevant tectonic structures in the study area.

[16] The thrust pattern of both profiles can be simplified to four structural domains (Figure 2), which are separated by thrusts observed in both profiles. Additionally, domains of local faulting and closely spaced thrusts exist in the Entlebuch. Tectonic Slice (TS) 1 represents all analyzed units south of the basal Alpine thrust. The northern limit of TS-2 is the basal UMM thrust, which also forms the southern limit of the triangle zone. TS-3 is the triangle zone itself, and TS-4 represents the Plateau Molasse with 4a being the folded and tilted proximal part and 4b the tectonically undisturbed flat-lying part (Figure 2).

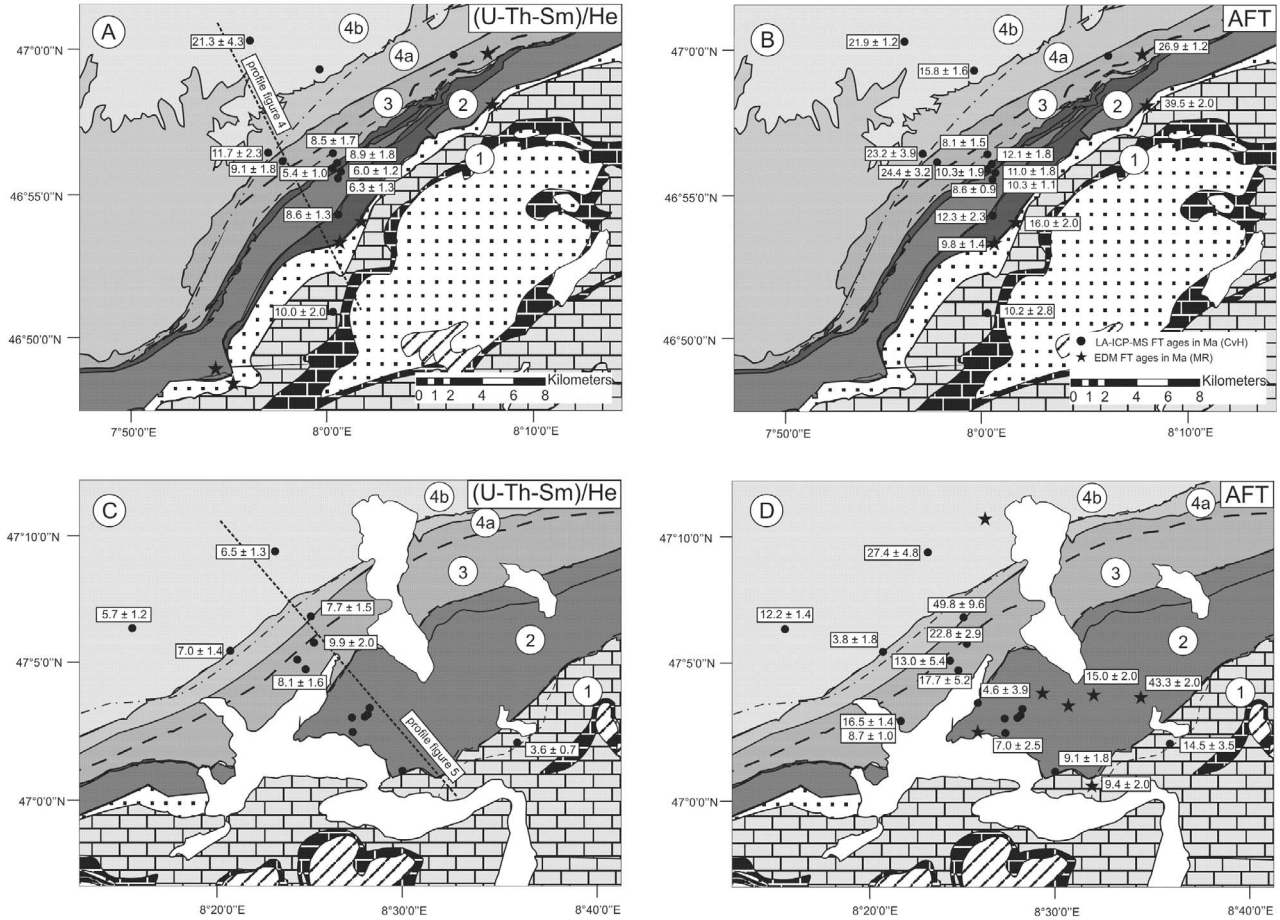

Figure 3. Detailed maps of the Entlebuch and Rigi areas and their corresponding thermochronology data. (a) Mean (U-Th-Sm)/He ages in the Entlebuch, (b) central apatite fission track ages from the Entlebuch area, (c) mean (U-Th-Sm)/He ages from the Rigi Mountain, and (d) central apatite fission track ages from the Rigi area. All ages in Ma. LA-ICP-MS, laser ablation–inductively coupled plasma–mass spectrometry; FT, fission track; EDM, external detector method; MR, analyst Meinert Rahn.

[17] One important difference between the two profiles as seen in map view is the greater apparent thickness of the UMM in Entlebuch, which is almost entirely absent in the Rigi area, even though the sediment thickness of the UMM increases southward and eastward [*Kuhlemann and Kempf*, 2002]. Hence, the Molasse at the Entlebuch section was either more deeply eroded and/or exhumed from deeper levels.

3. Methods

3.1. Sampling Strategy

[18] We collected thermochronometric samples along two horizontal profiles that span the entire folded and thrusted proximal part of the Molasse Basin, from Alpine Flysch units in the south to the tectonically undisturbed, flat-lying Plateau Molasse in the north (Figures 4 and 5). We collected samples in similar structural positions along both profiles (Figures 2 and 3) In the Entlebuch horizontal profile, sampling started in the south in the "Globigerinenschiefer" (Südelbach series, upper Eocene). We sampled along the N-S striking, deeply incised Waldemme Valley and finally reached the Napf Mountain farther north, where OSM alluvial fan conglomerates (11–7 Ma (F. Schlunegger, Geologische Karte Schüpfheim mit Erläuterungen, unpublished map, 2010)) are exposed. We collected samples at an approximate elevation of 800 m. All samples from the Entlebuch vertical profile were separated from cuttings from the Entlebuch-1 borehole. Because of little available material, each sample represents 15–20 m of well section. In the Rigi horizontal section, the sampling strategy was similar to Entlebuch. The sampled transect encompasses the North Helvetic Flysch (Altdorfer Sandstone, lower Oligocene) in the south to the OSM fluvial deposits of Tortonian age in the north. We collected samples at an approximate elevation of 500 m. In addition, at the west face of the Rigi Mountain, samples were collected from a subvertical profile, ranging from 630 m to 1750 m. Where possible, we selected granitic or sedimentary boulders in order to minimize effects of different time-temperature histories prior to deposition into the Molasse basin. Table S3 in the auxiliary material contains all geographical information (latitude, longitude and elevation).[1]

[1]Auxiliary materials are available in the HTML. doi:10.1029/2011TC003078.

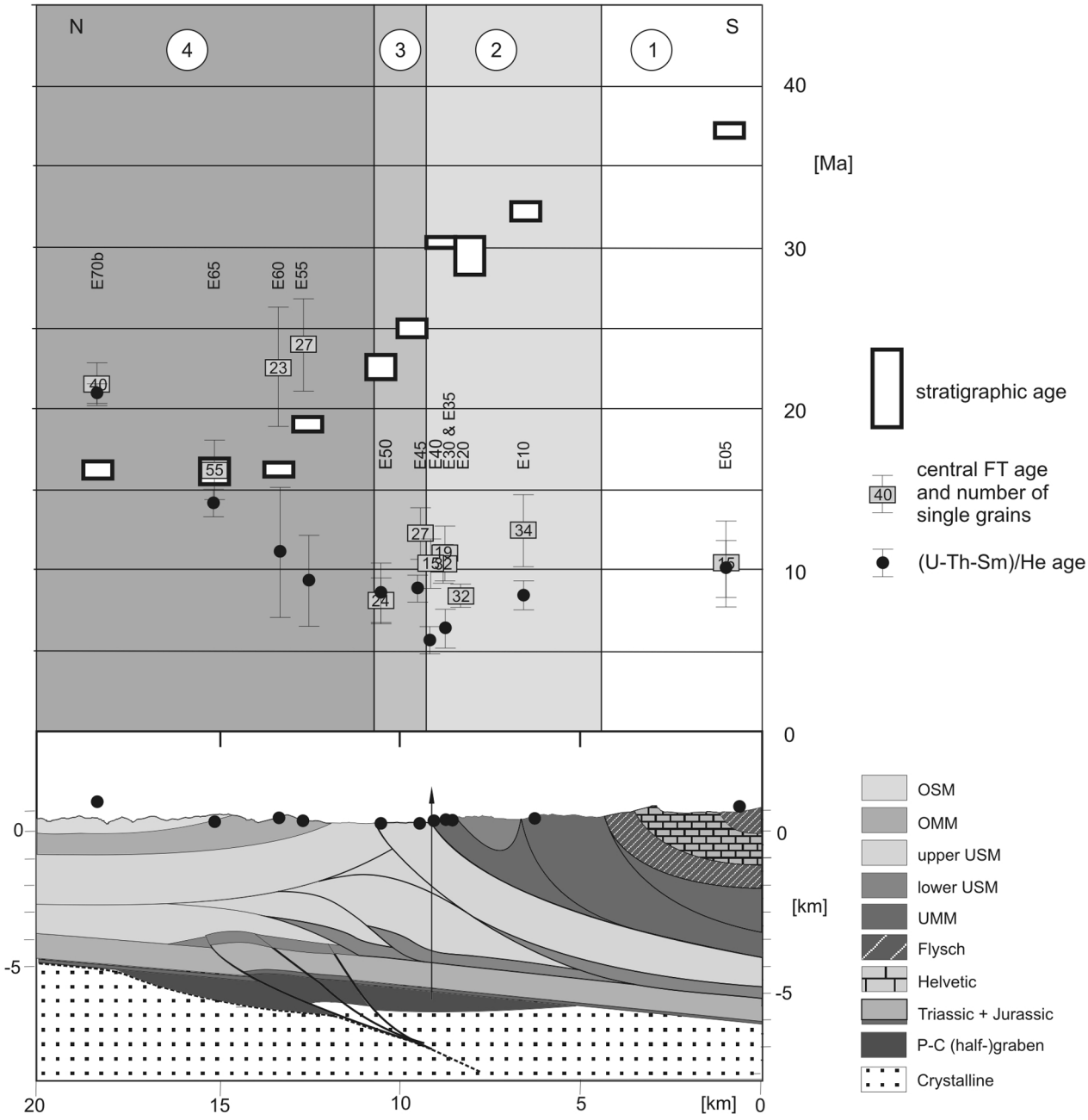

Figure 4. Profile across the Subalpine Molasse in the Entlebuch area, Switzerland. For location of cross section, see dashed line in Figure 3a. Black dots in cross section below indicate the projected sampling localities. The tectonic slices are as defined in Figure 2. In the south, all samples show ages significantly younger ages than their stratigraphic ages, whereas in the north the opposite is observed. Hence, an exposed paleopartial annealing zone and partial retention zone reaches the surface in the tectonic slices south of TS-4. P-C, Permo-Carboniferous.

3.2. Fission Track and (U-Th-Sm)/He Principles and Methods

[19] The AFT and (U-Th-Sm)/He dating methods are based on two different physical processes and cover different temperature intervals. The AFT technique records cooling in the range of ~120–60°C [*Carlson et al.*, 1999], whereas the (U-Th-Sm)/He method detects cooling events in the range of ~80–40°C [*Wolf et al.*, 1996; *Flowers et al.*, 2009]. These temperature ranges are called the partial annealing zone and the partial retention zone, respectively. Note that all presented ages are cooling ages, thus representing the point in time, when an apatite grain within the sample passed through its individual closure temperature. Rapidly cooled samples will feature similar AFT and (U-Th-Sm)/He ages. In areas experiencing slower cooling, the two thermochronometer ages will differ [e.g., *Fitzgerald et al.*, 2006]. Combined, the

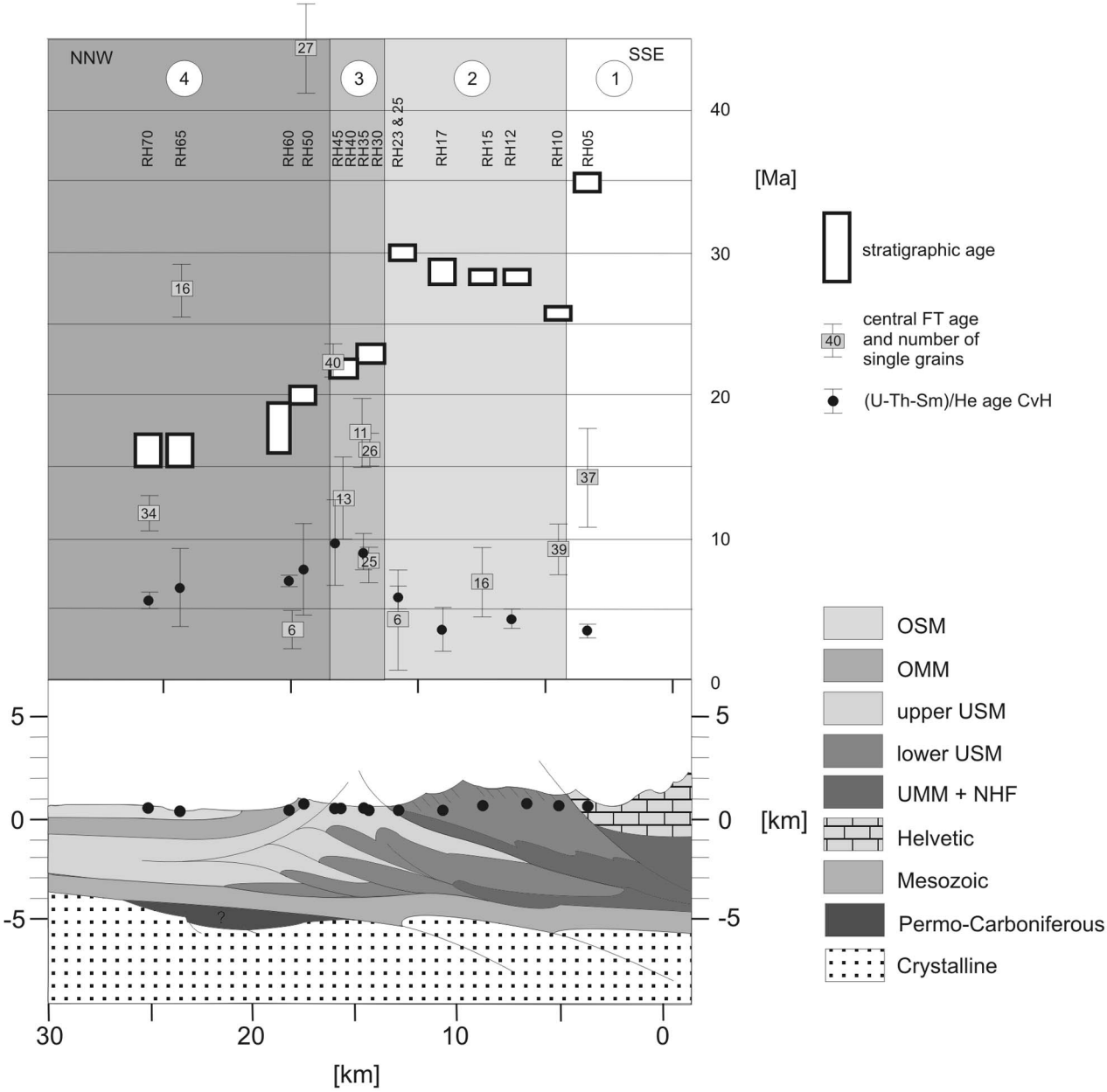

Figure 5. Profile across the Subalpine Molasse in the Rigi area, Switzerland. For location of cross section, see line R in Figure 1. Legend and data pattern are as in Figure 5. Note that in contrast to the Entlebuch profile, the apatite (U-Th-Sm)/He and apatite fission track ages experienced some annealing/He loss within the basin including the area north of the triangle zone.

two techniques provide a powerful means to decipher low-temperature cooling histories [*Armstrong et al.*, 2003; *Stockli*, 2005]. For fission track dating, the uranium content of the dated grains can be determined in two ways, either by an external detector or by laser ablation–inductively coupled plasma–mass spectrometry (laser ablation), which we applied in this study. For more detailed information about the methods and their application, the reader is referred to Text S1 in the auxiliary material.

[20] We performed AFT analyses on 31 samples. We extracted and concentrated the apatite crystals by using a standard combination of heavy liquid and magnetic separation techniques (see the auxiliary material). Where possible, we produced 40 single grain ages for every sample. Age and standard measurements are summarized in Table 1. From three sampling locations, we chose several boulders of potentially different origin that experienced a common postdepositional time-temperature history. We treat each boulder as an individual sample. From the new data, one sample (RV10b) is not considered further. From 21 grains, only four have sufficient uranium for a meaningful age, and most of them have zero spontaneous tracks.

[21] For the vertical sections close to the Rigi and the Entlebuch sections and some locations in the basin, ages

Table 1. Results of Apatite Fission Track Dating From the Subalpine Molasse, Switzerland, Using the Laser Ablation Method for ^{238}U Analysis[a]

Sample	Grains	Dpar (mm)	Ns	Area Analyzed (cm^2)	$\Sigma(P*\Omega)$ (cm^2)	1σ $\Sigma(P*\Omega)$ (cm^2)	ζMS	1σ ζMS	^{43}Ca bkg:sig	^{238}U bkg:sig	Q	Central Age (Ma)	1σ (Ma)	Age Dispersion (%)
E05	15	1.24	56	2.09E−04	0.65755	1.06E−02	192608	5.78E−01	216.78	23.57	0.00	10.2	2.75	34.6
E10	34	1.40	123	6.67E−04	1.4791	3.70E−02	192140	8.08E−01	239.49	76.55	0.00	12.3	2.25	24.6
E20	32	1.26	93	9.18E−04	1.2717	1.51E−02	189357	7.61E−01	215.57	18.31	0.55	8.6	0.90	0.0
E30	32	1.40	163	1.30E−03	1.6831	2.30E−02	188361	1.64E+04	234.27	33.49	0.04	10.3	1.11	12.6
E35	19	1.24	71	3.80E−04	0.80586	1.52E−02	193111	8.24E−01	217.56	41.03	0.06	11.0	1.76	14.2
E40	19	1.23	551	3.85E−04	1.178	3.59E−02	193825	8.36E−01	271.53	94.31	0.00	10.3	1.91	14.4
E45	27	1.32	210	8.90E−04	1.8422	2.54E−02	186681	1.08E+04	214.94	21.76	0.00	12.1	1.76	23.0
E50	24	1.18	88	6.69E−04	1.2643	1.35E−02	195509	8.64E−01	219.41	17.10	0.00	8.1	1.49	30.1
E55	27	1.26	249	6.03E−04	1.1395	2.01E−02	196480	8.81E−01	207.99	86.96	0.00	24.4	3.23	13.9
E60	23	1.25	123	4.47E−04	0.63711	8.28E−03	194631	8.50E−01	230.19	520.92	0.00	23.2	3.92	17.7
E65	55	1.30	265	1.87E−03	2.01	3.60E−02	192693	9.42E−01	261.68	426.53	0.00	15.8	1.64	16.1
E70b	40	1.42	522	6.00E−04	2.3632	1.95E−02	188950	1.84E+04	252.05	26.54	0.00	21.9	1.24	6.3
RH05	37	1.28	113	7.24E−04	1.1488	1.51E−02	185959	8.33E−01	239.23	143.75	0.00	14.5	3.50	31.4
RH10	39	1.18	25	1.11E−03	0.55854	5.95E−03	190315	5.88E−01	283.77	46.48	0.84	9.1	1.75	0.0
RH15	16	1.32	10	2.37E−04	0.37926	9.91E−03	190907	5.85E−01	255.18	205.76	0.19	7.0	2.52	25.2
RH25	6	1.14	3	1.01E−04	0.19965	7.50E−03	191408	7.96E−01	203.92	6.65	0.12	4.6	3.93	70.1
RH30a	26	1.29	198	4.30E−04	1.5115	3.19E−02	189618	5.91E−01	244.96	75.60	0.00	16.5	1.35	5.7
RH30b	25	1.17	148	4.63E−04	2.187	3.30E−02	188615	5.95E−01	220.58	53.81	0.00	8.7	1.02	16.0
RH35	11	1.40	33	1.89E−04	0.23082	4.41E−03	211879	5.85E−01	275.75	181.76	0.00	17.7	5.15	17.6
RH40	13	1.28	8	2.78E−04	0.11016	3.08E−03	211879	5.85E−01	266.01	465.53	0.03	13.0	5.35	10.4
RH45	40	1.25	331	1.28E−03	1.8253	2.20E−02	189796	2.12E+04	235.95	108.21	0.00	22.8	2.93	19.4
RH50	27	1.38	150	5.54E−04	0.39386	6.88E−03	187571	1.37E+04	221.40	40.81	0.00	49.8	9.62	20.3
RH60c	6	1.16	4	1.28E−04	0.12542	3.21E−03	190053	7.73E−01	223.49	11.00	1.00	3.8	1.83	0.0
RH65	16	1.29	118	5.43E−04	0.56082	2.11E−02	188633	1.73E+04	246.11	189.92	0.11	27.4	4.83	9.1
RH70	34	1.39	214	1.26E−03	1.8217	2.03E−02	189373	1.98E+04	213.98	48.65	0.00	12.2	1.43	16.9
RV15	12	1.10	31	1.73E−04	0.092727	2.08E−03	190401	7.79E−01	198.89	21.77	0.00	27.9	12.80	22.4

[a]Dpar is the arithmetic mean maximum diameter of fission track etch figures, Ns is the number of spontaneous tracks counted, $P = {}^{238}U/{}^{43}Ca$ and Ω are area for a single apatite grain, ζMS is the zeta value for laser ablation dating, and Q is the χ^2 probability. Central ages were calculated using the RadialPlotter software by *Vermeesch* [2009]; bgk:sig is the background signal during measurement of ^{43}Ca and ^{238}U, respectively.

produced with the external detector method were added to the data set and compared to the data where the uranium content was determined by laser ablation (see section 4.6). We took previously published data from *Cederbom et al.* [2004]. Unpublished ages dated with the external detector method were counted by M. Rahn and are listed in Table 2.

[22] We present the so-called peak AFT and the central ages, which represent either the age of a grain age population obtained by RadialPlotter [*Vermeesch*, 2009] or the whole sample age, respectively [*Galbraith*, 2005]. For completely annealed samples, the peak age and the central age are identical; for samples with more than one grain age population, the central age provides information about trends within the data set and is statistically robust. Grain age populations are defined by minimizing the Bayesian Information Criterion [*Vermeesch*, 2009]. Radial plots for all dated AFT samples are provided in Figures S1–S5 in the auxiliary material. We use the presence of peak ages only as a measure whether the sample was completely reset (i.e., experienced temperatures higher than their closure temperature).

[23] In addition, we present 18 mean (U-Th-Sm)/He ages. For all samples three to six aliquots were analyzed (Table 3). Raw (U-Th-Sm)/He ages were corrected for alpha ejection at the crystal surfaces. In this study, we use the weighted mean age. Mean age and error calculation are discussed in the auxiliary material.

4. Results

[24] Here, we present the ages obtained with the laser ablation inductively coupled mass spectrometry method (Table 1), the external detector method (Table 2), the (U-Th-Sm)/He data (Table 3) and the peak ages of the AFT data (Table 4) in individual sections. We compare the two data sets and present cooling histories generated by inverse

Table 2. Results of Apatite Fission Track Dating From the Subalpine Molasse, Switzerland, Using the External Detector Method for U Analysis[a]

Sample	Location	Grains (Dimensionless)	Ns (Number of Tracks)	Ni (Number of Tracks)	rhoD (10^6 Tracks/cm^3)	$P(\chi^2)$	Central Age (Ma)	Age Dispersion (%)
MR P179	Flühli	23	53	982	1,061E + 06	0,46	9.80 ± 1.4	0
MR P198	Fischenbach	40	769	5014	1,025E + 06	0,28	26.9 ± 1.2	0

[a]Ns and Ni are the numbers of spontaneous and induced tracks counted, respectively, rhoD is the density of tracks on the dosimeter glass mica (corresponding to 12 ppm U), and $P(\chi^2)$ is the value indicating whether the data show extra Poissonian variations (i.e., if they are overdispersed due to experimental or geological factors [*Tagami and O'Sullivan*, 2005]. For age calculation, a ζ(CN5) of 343 ± 5 (MR) was used.

Table 3. Apatite (U-Th-Sm)/He Dating Results From the Subalpine Molasse, Switzerland[a]

Sample	Elevation (masl)	Mass (μg)	U (ppm)	Th (ppm)	eU (ppm)	Sm (ppm)	4He (nmol/g)	Ft	Raw Age (Ma)	Corrected Age (Ma)	Error (Ma)	Series	Excluded Age	Mean Age (Ma)	Error (Ma)
E05-1	1140	12.68	98.69	70.29	115.22	70.21	7.11	0.78	11.38	14.62	0.88	(B)			
E05-2		2.28	16.11	15.91	20.56	157.94	3.05	0.68	26.66	39.25	2.35		e		
E05-3		4.28	61.85	9.87	64.94	162.59	2.19	0.73	6.19	8.46	0.51			10.01	2.00
E05-4		1.86	381.77	207.99	726.12	59293.54	102.15	0.67	20.59	30.94	16.72		e		
E05-5		2.83	74.44	637.79	222.24	196.99	8.67	0.68	7.07	10.33	0.08		e		
E10-1	845	1.48	49.26	373.62	137.79	504.58	2.50	0.69	3.35	5.01	0.11	(A)	e		
E10-2		5.09	56.60	460.41	164.81	445.13	4.96	0.77	5.53	7.37	0.11		e		
E10-3		4.97	23.01	1377.17	342.74	541.33	3.75	0.78	1.99	2.63	0.04		e		
E10-4		9.60	20.10	3.69	21.45	101.29	0.78	0.80	6.85	8.55	0.17			8.55	1.33
E30-1	800	4.15	19.66	150.49	54.71	82.06	1.32	0.70	4.37	6.25	0.37	(A)			
E30-2		2.12	10.89	61.87	25.29	32.41	0.56	0.65	4.03	6.18	0.37				
E30-3		5.72	16.82	102.46	41.03	125.78	1.09	0.74	4.81	6.47	0.39			6.30	1.26
E35-1	785	8.66	20.03	36.43	29.07	130.99	0.75	0.82	4.82	5.95	0.11	(B)		5.95	1.19
E40-1	772	10.96	51.90	36.22	61.15	183.64	3.04	0.81	9.29	11.53	0.20	(A)			
E40-2		1.89	173.74	41.26	185.05	361.24	4.29	0.70	4.32	6.19	0.12				
E40-3		5.87	11.15	29.40	19.36	287.47	0.42	0.79	4.23	5.42	0.11				
E40-4		31.42	7.98	20.23	13.06	84.71	0.27	0.88	3.88	4.45	0.07				
E40-5		12.45	21.96	18.16	27.44	260.52	0.63	0.82	4.36	5.32	0.09			5.37	1.07
E45-1	758	2.28	28.19	58.25	42.56	192.12	1.24	0.65	5.29	8.10	0.49	(B)			
E45-2		2.76	40.14	41.27	49.84	39.04	1.66	0.69	6.11	8.86	0.53				
E45-3		2.08	57.13	27.14	64.10	143.08	2.42	0.67	6.94	10.33	0.62			8.92	1.78
E50-1	745	6.06	0.09	0.05	0.10	0.02	0.00	0.79	0.00	0.00	NA[b]	(A)	e		
E50-2		6.66	25.90	34.09	35.95	440.44	1.10	0.80	5.91	7.42	0.12				
E50-3		7.17	10.69	8.35	13.66	209.58	0.51	0.80	7.27	9.18	0.22				
E50-4		8.09	41.25	7.24	44.10	236.07	2.06	0.79	8.82	11.19	0.21			8.53	1.71
E55-1	800	5.93	20.15	28.21	27.75	222.15	0.88	0.79	6.02	7.68	0.15	(A)			
E55-2		8.74	2.68	55.33	15.64	45.10	2.78	0.82	32.52	40.68	0.66		e		
E55-3		5.99	21.42	22.54	28.09	295.56	1.37	0.79	9.38	11.90	0.21			9.05	1.81
E60-1	970	5.27	34.41	7.27	36.47	77.13	1.71	0.78	8.76	11.30	0.22	(A)			
E60-2		6.91	22.55	38.57	32.51	216.68	2.88	0.79	16.73	21.28	0.33				
E60-3		5.16	7.47	16.77	12.10	155.27	0.33	0.78	5.20	6.72	0.15				
E60-4		2.95	21.83	25.65	28.42	136.98	1.88	0.73	12.39	17.16	0.32				
E60-5		7.02	12.11	19.66	17.00	73.23	1.32	0.80	14.54	18.35	0.29			11.68	2.34
E65-1	773	5.72	0.22	7.77	2.03	2.59	2.93	0.77	259.86	348.96	7.15	(A)	e		
E65-2		3.30	68.93	16.55	76.17	686.03	0.00	0.77	0.00	0.00	NA[b]		e		
E65-3		5.57	33.49	11.85	37.35	227.01	2.24	0.80	11.34	14.20	0.25				
E65-4		1.50	12.43	14.11	16.40	144.23	0.89	0.63	9.76	15.49	0.93				
E65-5		4.62	0.16	1.16	0.44	1.67	0.01	0.72	2.08	2.87	0.17		e		
E65-6		3.63	29.17	12.68	32.72	126.66	2.27	0.72	12.68	17.61	1.06				
E65-7		3.12	25.76	17.93	30.71	165.48	2.16	0.71	12.76	17.90	1.07				
E65-8		3.19	26.89	18.03	31.30	51.53	2.34	0.71	13.74	19.43	1.17			14.80	2.96
E70b-1	1325	1.10	87.24	73.73	104.76	109.39	10.55	0.60	18.51	30.86	1.85	(B)	e		
E70b-2		1.18	87.43	76.97	106.04	177.88	7.81	0.61	13.52	22.05	1.32				
E70b-3		0.98	49.18	90.88	70.87	153.64	4.67	0.56	12.03	21.46	1.29				
E70b-4		3.71	81.57	72.51	99.07	160.19	8.33	0.73	15.44	21.26	0.30			21.31	4.27
E3-1-1	420–435	3.32	31.00	6.04	32.84	89.44	0.86	0.71	4.82	6.75	0.40	(B)			
E3-1-2		1.80	31.32	50.98	43.53	94.64	1.22	0.65	5.13	7.86	0.47				
E3-1-3		1.06	14.81	39.57	25.02	218.89	0.70	0.57	4.97	8.71	0.52			7.61	1.52
E3-2-1	1210–1230	1.10	52.29	9.92	55.04	93.46	0.58	0.62	1.95	3.17	0.19	(B)			
E3-2-2		1.93	61.61	55.75	74.95	101.71	2.08	0.66	5.11	7.69	0.46				
E3-2-3		2.00	5.08	21.46	10.40	76.07	0.34	0.65	5.84	8.96	0.54			4.32	0.86
E3-2.5-1	1415–1435	1.01	41.35	94.42	63.77	136.04	1.33	0.56	3.80	6.78	0.41	(B)			
E3-2.5-2		1.01	99.36	84.06	119.43	144.33	1.35	0.59	2.08	3.53	0.21				
E3-2.5-3		0.97	33.40	47.95	44.87	86.51	0.37	0.57	1.49	2.61	0.16			3.27	0.65
E3-3-1	1615–1635	2.56	24.0	26.1	30.2	49.1	1.09	0.7	4.03	6.0	0.48	(B)			
E3-3-2		5.78	48.8	36.6	57.4	42.4	0.75	0.8	2.65	3.3	0.27				
E3-3-3		4.10	17.6	7.9	19.6	44.4	0.45	0.3	0.93	3.5	0.28			3.76	0.75
E3-4-1	1820–1840	0.97	54.6	121.7	82.8	33.3	2.23	1.3	6.23	5.0	0.40	(B)			
E3-4-2		1.94	1.2	2.0	1.7	0.5	1.70	270	NA[b]	NA[b]	NA[b]		e		
E3-4-3		2.24	41.7	66.0	57.3	80.3	1.58	0.1	0.05	0.5	0.04		e	4.97	0.99
E3-5-1	2110–2130	1.96	24.05	42.05	33.97	47.61	0.35	0.66	1.88	2.85	0.17	(B)			
E3-5-2		1.54	59.66	79.60	78.80	164.65	0.62	0.63	1.43	2.27	0.14				
E3-5-3		4.11	21.70	9.13	24.00	39.92	0.73	0.73	5.63	7.77	0.47		e	2.49	0.50
RH05-1	620	3.52	8.91	223.65	60.66	52.65	0.71	0.69	2.11	3.05	0.18	(B)			
RH05-2		1.73	30.12	67.68	46.48	156.83	0.57	0.62	2.25	3.63	0.22				
RH05-3		1.11	29.94	345.87	110.12	111.50	1.66	0.58	2.73	4.73	0.28			3.57	0.71
RH12-1	735	9.81	36.3	160.8	73.6	58.5	1.3	0.79	3.29	4.2	0.33	(B)			
RH12-2		9.14	41.2	167.5	80.1	65.3	1.5	0.78	3.45	4.4	0.35				
RH12-3		5.29	0.7	0.8	0.9	0.2	4.3	0.75	827.10	1103.3	88.26		e	4.29	0.86
RH17-1	461	2.10	122.1	43.5	132.5	71.4	4.2	0.68	5.92	8.7	0.70	(B)			

Table 3. (continued)

Sample	Elevation (masl)	Mass (μg)	U (ppm)	Th (ppm)	eU (ppm)	Sm (ppm)	4He (nmol/g)	Ft	Raw Age (Ma)	Corrected Age (Ma)	Error (Ma)	Series	Excluded Age	Mean Age (Ma)	Error (Ma)
RH17-2		1.30	11.2	376.9	98.3	50.4	1.0	0.60	1.81	3.0	0.24				
RH17-3		1.68	19.7	108.2	45.0	67.4	0.6	0.63	2.24	3.5	0.28			3.59	0.72
RH23-1	383	2.10	7.5	39.7	16.8	20.6	1.0	0.65	10.94	16.8	1.34	(B)	e		
RH23-2		3.08	4.2	11.2	7.0	39.9	0.1	0.70	3.80	5.4	0.43				
RH23-3		4.91	8.5	16.2	12.4	27.3	0.3	0.73	4.64	6.3	0.51			5.80	1.16
RH35-1	562	3.47	14.71	38.50	23.85	57.23	0.95	0.71	7.24	10.25	0.61	(B)			
RH35-2		2.28	31.18	44.64	41.61	31.15	1.12	0.67	4.93	7.37	0.44				
RH35-3		3.30	19.96	44.02	30.37	55.28	0.90	0.71	5.41	7.64	0.46			8.08	1.62
RH45-1	535	3.71	43.95	81.04	63.27	133.00	2.19	0.71	6.32	8.94	0.54	(B)			
RH45-2		6.19	136.19	11.87	139.43	102.01	17.24	0.78	22.85	29.47	1.77		e		
RH45-3		5.91	62.03	10.42	64.91	95.36	2.48	0.77	7.05	9.15	0.55				
RH45-4		3.34	105.16	16.10	109.37	98.95	17.45	0.73	29.45	40.39	2.42		e		
RH45-5		6.61	59.57	24.41	65.72	105.39	3.73	0.77	10.46	13.50	0.81			9.86	1.97
RH50-1	740	2.09	5.50	25.71	11.64	44.46	0.52	0.65	8.00	12.36	0.74	(B)			
RH50-2		2.06	88.48	289.36	155.47	74.83	3.62	0.66	4.25	6.45	0.39				
RH50-3		0.89	67.78	65.45	84.29	288.87	2.05	0.58	4.44	7.65	0.46			7.69	1.54
RH60c-1	465	1.05	17.09	144.31	52.09	356.10	2.48	0.57	8.47	14.86	0.89	(B)	e		
RH60c-2		2.70	9.56	92.75	32.31	280.91	0.95	0.67	5.20	7.71	0.46				
RH60c-3		1.99	9.41	126.06	40.37	388.06	0.96	0.65	4.17	6.46	0.39			6.97	1.39
RH65-1	450	2.37	2.69	9.85	5.64	136.49	0.10	0.66	3.12	4.72	0.28	(B)			
RH65-2		2.34	87.27	30.09	94.58	76.78	2.72	0.68	5.32	7.80	0.47				
RH65-3		1.65	5.47	13.56	9.16	113.34	0.87	0.63	16.70	26.35	1.58		e		
RH65-4		0.80	16.01	60.81	30.68	134.89	0.45	0.55	2.67	4.88	0.20				
RH65-5		3.95	16.97	40.85	26.71	67.03	0.88	0.72	6.00	8.32	0.18			6.49	1.30
RH70-1	523	2.73	25.61	32.05	33.10	20.81	0.88	0.69	4.87	7.03	0.42	(B)			
RH70-2		2.77	25.09	39.05	34.62	107.72	0.67	0.69	3.50	5.06	0.30				
RH70-3		2.79	22.36	35.83	30.87	51.68	0.67	0.69	3.96	5.72	0.34			5.73	1.15
RV10b-1	1520	5.05	150.21	111.69	204.92	5799.02	0.38	0.75	0.31	0.42	0.03	(B)	e		
RV10b-2		1.28	30.95	81.23	80.14	6098.94	0.17	0.61	0.31	0.51	0.03		e		
RV10b-3		5.07	0.85	1.53	1.24	7.74	0.18	0.74	25.57	34.35	2.06			34.35	6.87
RV15-1	1405	2.23	24.65	134.95	57.74	404.00	1.68	0.67	5.20	7.81	0.47	(B)			
RV15-2		1.26	14.40	59.38	30.06	398.67	0.80	0.61	4.69	7.74	0.46				
RV15-3		2.16	13.74	46.84	27.41	577.83	1.32	0.66	8.28	12.53	0.75			8.54	1.71
RV25-1	1335	2.97	2.63	102.66	26.45	37.75	0.51	0.68	3.49	5.09	0.31	(B)			
RV25-2		5.14	2.04	3.00	2.89	30.78	0.10	0.75	6.22	8.32	0.50			5.97	1.19
RV30c-1	1040	1.22	13.19	55.29	26.33	84.12	0.71	0.59	4.86	8.25	0.50	(B)			
RV30c-2		2.15	43.40	53.42	56.12	82.70	1.62	0.66	5.31	8.06	0.48				
RV30c-3		3.25	33.25	78.61	51.44	18.71	1.87	0.70	6.66	9.47	0.57			8.51	1.70

[a]Elevation is given in meters above sea level (masl); eU is the effective uranium concentration, which weights the decay of the parents for their alpha productivity [*Flowers et al.*, 2009]; Ft is the α ejection correction factor; Series denotes the lab in which the grains were analyzed (see auxiliary material for details); excluded ages have not been taken into account for the geological interpretation for reasons given in the text and in the auxiliary material.
[b]NA, not available.

modeling of the two combined data sets. All samples have, like the tectonic slices, increasing numbers from south to north. We discuss them in the following in that order.

4.1. AFT Age Distribution

4.1.1. Entlebuch Horizontal Section

[25] Figure 3b shows all sample locations and their corresponding central AFT age. Figure 4 presents the central age and the corresponding stratigraphic age along the horizontal section. For quality control, we produced AFT ages for two separate samples from the same location. Samples E30 and E35 were collected close to the northern fringe of TS-2, south of a minor thrust (Figure 3b), within an area where at least partially annealed samples are expected based on previous studies [*Cederbom et al.*, 2004, 2011]. The central ages obtained are 10.3 $\pm$ 2.2 Ma and 11.0 $\pm$ 3.5 Ma respectively, reproducing well within error. One single grain age population is sufficient for minimizing the Bayesian Information Criterion for both samples.

[26] AFT ages within domains TS-1 to TS-3 (samples E05–E35) range between 8.1 to 12.3 Ma. These southern samples are all much younger than the corresponding stratigraphic age, and accordingly must have resided within the partial annealing zone after deposition. In the northern part of the section, AFT ages are older than the corresponding stratigraphic age. The potential low-temperature boundaries of the exhumed fossil partial annealing zone are located at the northern termination of the triangle zone (Figure 4).

[27] Within this general pattern, analyzing grain age distributions using radial plots yields additional information. Radial plots for all samples are given in Figures S1–S5 the auxiliary material. Not all single grain ages plot within the 2σ error bars, indicating the potential presence of more than one population. However, for small age dispersions random effects may also cause this. Hence, we do not interpret peak ages that are due to one or two grains.

[28] Sample E05 is significantly younger than its stratigraphic age, indicating strong partial or total annealing. The

Table 4. Peak Ages for All New Apatite Fission Track Ages From the Subalpine Molasse, Switzerland[a]

Sample	Number of Grains	Peak 1 (Ma)	Grain Portion (%)	Peak 2 (Ma)	Grain Portion (%)	Peak 3 (Ma)
E05	15	10.1	84.4	43.4	15.6	
E10	34	5.1	36.7	20.9	63.3	
E20	32	8.6	100			
E30	32	6.0	21.1	12.1	78.9	
E35	19	6.6	38.1	15.5	61.9	
E40	19	2.9	13.2	12.7	86.8	
E45	27	7.8	57.0	16.9	34.3	48.8
E50	24	3.5	40.7	14.2	59.3	
E55	27	17.6	50.9	38.1	49.1	
E60	23	8.2	25.4	32.4	74.6	
E65	55	11.0	68.3	30.8	31.7	
E70b	40	22.2	100			
RH05	37	9.6	72.2	51.1	27.8	
RH10	39	9.1	100			
RH15	16	6.9	100			
RH25	6	3.5	100			
RH30a	26	16.6	100			
RH30b	25	9.4	100			
RH35	11	8.6	43.6	29.5	56.4	
RH40	13	13.8	100			
RH45	40	14.4	52.1	30.0	39.4	121.0
RH50	27	30.0	72.4	176.0	27.6	
RH60c	6	3.8	100			
RH65	16	22.8	100			
RH70	34	6.1	29.9	16.1	70.1	
RV15	12	14.5	76.5	87.2	23.5	
RV20	21	7.5	74.8	71.0	25.2	
RV25	18	17.1	100		0.0	
RV30a	30	9.9	76.8	76.4	23.2	
RV30b	27	9.3	69.5	81.0	30.5	
RV30c	27	14.1	55.7	46.4	44.3	

[a]The presence of different grain age populations is not interpreted any further but is used as indication for (partial) resetting and as quality control for reproducibility. For graphic representation of peak ages, see Figures S1–S5 in the auxiliary material.

43.4 Ma peak age is based on one single grain age only. In E10, two grain age populations are identified, yielding ages of 20.9 and 5.1 Ma respectively (Table 4). The two age populations correlate with Dpar, the grains of the older peak having Dpar $\geq$ 2.2 μm, and the younger grains being associated with Dpar $\leq$ 1.5 μm (see radial plots in the auxiliary material).

[29] Sample E20 (TS-2) has only one grain age population and a central age of 8.6 $\pm$ 1.8 Ma, indicating total annealing. E40, as the northernmost sample of TS-2, has a central fission track age of 10.3 $\pm$ 1.9 Ma, thus significantly younger than its corresponding stratigraphic age. The youngest peak age is based on one single grain age and this age is much younger than the corresponding (U-Th-Sm)/He age. Removing this grain from the data set results in a central age of 12.1 $\pm$ 3.8 Ma. In summary, all samples in TS-1 and TS-2 have been strongly or totally annealed since deposition.

[30] For sample E45 (TS-3), collected just north of the basal UMM thrust, yields a central age of 12.1 $\pm$ 3.5 Ma. Three distinct grain age populations are observed, one of which is older than its stratigraphic age (Table 4). The single grain age distribution suggests that sample E45 has not been totally annealed and has thus not experienced temperatures as high as sample E40 south of the basal thrust of the Subalpine Molasse.

[31] At the northern fringe of TS-3, sample E50 yields a central age of 8.1 $\pm$ 3.0 Ma, which is slightly younger than ages farther to the south. Two grain age populations are 14.2 Ma and 3.5 Ma, respectively (Table 4). A weak correlation between Dpar and single grain ages in E45 and no such correlation in E50 suggest that sample E50 is closer to total annealing and has hence probably experienced higher temperatures than E45.

[32] In TS-4, central AFT ages (samples E55–E70b; Figure 4) are significantly older than in the other tectonic units. They are as old as or only slightly younger than their corresponding stratigraphic age. For this region, *Cederbom et al.* [2011] estimated 1.4 to 2.1 km of erosion, indicating partial annealing of the samples in the south of TS-4. Within the fossil partial annealing zone, small changes in elevation may have a large impact on AFT ages. This potentially explains why E65 yields a younger age than E60 (15.8 $\pm$ 3.2 and 23.2 $\pm$ 7.8 Ma sampled at elevations of 773 and 970 m respectively, Table S3), even though its corresponding stratigraphic age is younger.

4.1.2. Entlebuch Vertical Section

[33] The well Entlebuch-1 is located at the boundary between UMM and USM, i.e., within the triangle zone (TS-3) [*Vollmayr and Wendt*, 1987]. Fission track data of this vertical section have been published and discussed in more detail by *Cederbom et al.* [2011]. They show a younging trend of central AFT ages below ~1500 m depth. Furthermore, an offset in the partial annealing zone within the youngest grain age population exists (Figure 6), which Cederbom et al. interpreted as an indication of thrust reactivation during late cooling. This vertical section provides information about the location and vertical extension of the exhumed fossil partial annealing zone.

4.1.3. Rigi Horizontal Section

[34] Figure 3d shows sampling localities and corresponding central AFT ages. Similar to Entlebuch, central ages are presented together with corresponding stratigraphic age along the vertical transect in Figure 5. The central AFT ages in TS-1 and TS-2 are considerably younger than their corresponding stratigraphic age. Sample RH05 has a central age of 14.5 $\pm$ 7.0 Ma. Two grain age populations can be distinguished (9.6 and 51.1 Ma respectively), and they do not relate to differences in Dpar (Table 4). This indicates that the sample is partially, but not totally annealed. In the adjacent TS-2, the southernmost sample (RH10) has only one grain age population with a central age of 9.1 $\pm$ 3.5 Ma. In addition, grains with the highest Dpar values also have young single grain ages. Therefore, sample RH10 is regarded as totally annealed.

[35] Farther northward near the basal Rigi thrust, samples RH15 and RH25 show successively younger central AFT ages. The single grain AFT ages in each sample belong to a single population, indicating that both samples are totally annealed (Table 1).

[36] Within the triangle zone (TS-3), ages are older than in TS-2, but still younger than their corresponding stratigraphic ages (RH30a to RH45; Figure 5). Samples RH30a to RH40 are totally or strongly partially annealed. All samples except RH35 contain only one grain age population. The northernmost sample RH45 has a central age of 22.8 $\pm$ 5.9 Ma, which is similar to its stratigraphic age. Moreover, it is associated with three grain age populations, two of which

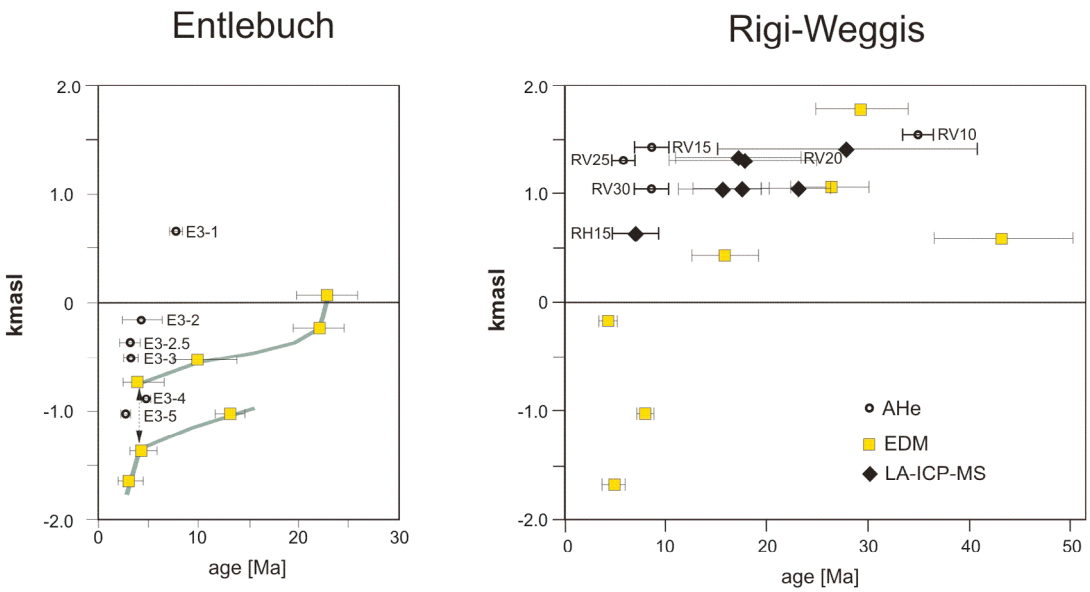

Figure 6. Vertical age profiles along (left) the Entlebuch well and (right) the Rigi Mountain and Weggis well with previously published and new data. Note the exhumed partial annealing–partial retention zone within both profiles and the offset between them. For details and comparisons between laser ablation and external detector method data, see discussion in the text.

are older than the stratigraphic age (Table 4). Hence, sample RH45 has probably experienced lower temperatures and less partial annealing than the samples farther south.

[37] In TS-4a, sample RH50 has a very old central age (45 Ma), with the youngest grain age population being older than the stratigraphic age. Evidently, the sample did not experience much heating after deposition. The central AFT age of sample RH60 is younger than the stratigraphic age (3.8 ± 3.6 Ma) but is based on six single grain age measurements only and has therefore to be considered with care. Sample RH65 has a central age of 27.4 ± 9.6 Ma, which is much older than the stratigraphic age. Accordingly, this sample did not experience enough reheating in the basin to reduce the AFT age significantly. RH70 shows a central age of 12.2 ± 2.8 Ma, which is slightly younger than its corresponding stratigraphic age. Its grain age distribution decomposes into two peak ages, which are 6.1 and 16.1 Ma and are correlated with Dpar values. Grain ages are younger than, and as old as the stratigraphic age respectively. This corroborates the finding of postdepositional cooling of more than 40°C within that area by *Cederbom et al.* [2004, 2011]. At 3 km north of sample RH70, the topmost sample in well Hünenberg-1 has not experienced any significant reheating since deposition [*Cederbom et al.*, 2011].

4.1.4. Rigi Vertical Section

[38] A subvertical profile from the western flank of Rigi Mountain (TS-2) is complemented by published AFT ages from a subvertical section on the eastern Rigi flank and by subsurface ages from the Weggis well (external detector method AFT ages from *Cederbom et al.* [2004]).

[39] Sample RV15 yields a central age of 27.9 ± 12.8 Ma at 1405 m. At the base of the Rigi Mountain (630 m), sample RH15 has a central age of 7.0 ± 2.5 Ma. All new central AFT ages are plotted in Figure 6, together with the previously published central AFT data. Together they illustrate a trend of decreasing ages from top to bottom. The age pattern corresponds to a fossil partial annealing zone, exhumed during early Pliocene times [*Cederbom et al.*, 2004].

[40] Independent evidence for a fossil partial annealing zone at Rigi is derived from the radial plots (Figures S1–S5). At an elevation of 1040 m, three samples (RV30a, RV30b and RV30c) were collected. Samples RV30a and RV30b originate from a calcareous sandstone, whereas RV30c is a sandstone boulder. Their central ages reproduce within 1σ error (Table 1), and samples RV30a and RV30b decompose into two similar grain age populations. The younger grain age populations (9.9 Ma and 9.3 Ma, respectively) are significantly younger than the corresponding stratigraphic age. A positive correlation exists between peak age and Dpar value in RV30b, indicating partial annealing of the samples.

4.2. (U-Th-Sm)/He Age Distribution

4.2.1. Entlebuch Horizontal Section

[41] We performed (U-Th-Sm)/He analyses for all samples (except E20) dated with the laser ablation AFT dating technique. Data are shown in Table 3 and plotted in Figures 3a and 4. The general trend is similar to the AFT data: young ages are obtained in the southern part of the Subalpine Molasse, whereas ages become successively older northward, including age trends within tectonic slices.

[42] The southernmost sample, E05, has a mean (U-Th-Sm)/He age of 10.0 ± 2.0 Ma. Since the sample is significantly younger than its corresponding stratigraphic age, complete resetting of the (U-Th-Sm)/He system can be inferred, in line with strong partial or total annealing of the AFT system. Following the profile northward, ages become progressively younger in TS-1 and TS-2.

[43] A clear jump in the age pattern is observed when crossing the basal UMM thrust into TS-3. Sample E45 and E50 have significantly younger stratigraphic ages

(20–25 Ma), but their mean (U-Th-Sm)/He ages are significantly older than those measured farther south (8.9 and 8.5 Ma respectively). Complete resetting of the (U-Th-Sm)/He system after deposition is probable in TS-3, since the single grain ages reproduce within uncertainty.

[44] In TS-4, the (U-Th-Sm)/He ages for sample E55 to E65 are younger that their stratigraphic ages, but show a spread in single grain ages, which cannot be explained only by methodological factors (see the auxiliary material). Instead, partial resetting is likely. In TS-4, the (U-Th-Sm)/He ages become older toward the north. The northernmost sample (E70b) has a (U-Th-Sm)/He age older than its corresponding stratigraphic age (Figure 4). Hence, the grains have not been significantly reheated in the partial retention zone after deposition.

4.2.2. Entlebuch Drill Hole Section

[45] At a depth of 425 m below surface, an age of 7.6 $\pm$ 1.5 Ma is measured, which is significantly younger than its stratigraphic age. Toward greater depths, ages become younger, indicating the (lower termination of the) fossil partial retention zone. An offset in this trend is observed between sample E3-3 and E3-4 (Figure 6). This offset coincides with the offset in central AFT ages.

4.2.3. Rigi Horizontal Section

[46] The (U-Th-Sm)/He analyses (Table 3 and Figures 3c and 5) were performed for most of the samples dated by laser ablation AFT technique. In TS-2, however, AFT and (U-Th-Sm)/He ages are measured on different samples. In general, all ages are young in comparison to the stratigraphic age and the oldest (U-Th-Sm)/He ages recorded in TS-3 (Figure 5).

[47] Similar to Entlebuch, the ages display characteristic age patterns within the tectonic slices. In TS-1 and TS-2, the (U-Th-Sm)/He ages are identical within error (3.6 $\pm$ 0.7, 4.3 $\pm$ 0.9 and 3.6 $\pm$ 0.7 Ma respectively). At the northern end of TS-2, an age of 5.8 $\pm$ 1.2 Ma is slightly older than the samples farther south (Figure 5). All ages are significantly younger than the corresponding stratigraphic ages, suggesting complete reset of the (U-Th-Sm)/He system.

[48] Older (U-Th-Sm)/He ages are observed in TS-3. Samples RH35 and RH45 have mean (U-Th-Sm)/He ages of 8.1 $\pm$ 1.6 Ma and 9.9 $\pm$ 2.0 Ma, respectively, thus reproduce within error. They are significantly younger than their stratigraphic ages, indicating total resetting. Their corresponding stratigraphic ages are significantly younger than those in TS-2.

[49] In TS-4, the (U-Th-Sm)/He ages are generally younger than in TS-3, and they become successively younger toward north. Similar to the AFT data, the age of the northernmost sample (RH70) is younger than the stratigraphic age of the sample, so the sample must have experienced postdepositional heating.

[50] In summary, very young (U-Th-Sm)/He ages exist south of the triangle zone, while the oldest ages are found within the triangle zone. In the Plateau Molasse, the ages are generally young, but only slightly younger than their stratigraphic ages. Similar to the Entlebuch, an age offset occurs across the basal UMM thrust.

4.2.4. Rigi Vertical Section

[51] The topmost sample (RV10b) from 1520 m, has a (U-Th-Sm)/He age of 34.4 $\pm$ 6.9 Ma, which is older than the stratigraphic age (however, with only one grain dated successfully). The relatively old age, if indeed representative, indicates that the sample was not fully reset and is located within or above the paleopartial retention zone. At 1405 m, the mean (U-Th-Sm)/He age is 8.5 $\pm$ 1.7 Ma. At 1335 m, the sample yields an age of 6.0 $\pm$ 1.2 Ma. At 1040 m the obtained age is 8.5 $\pm$ 1.7 Ma again. All these ages are significantly younger than the corresponding stratigraphic age, suggesting strong to complete resetting of the apatite (U-Th-Sm)/He system.

4.3. Comparison of Apatite (U-Th-Sm)/He and AFT Results

[52] Both thermochronometers indicate significant cooling in Mio-Pliocene times. Combining the two data sets provides additional information about the cooling histories.

[53] At Entlebuch (Figure 4), AFT ages in TS-1 and TS-2 are rather uniform. Corresponding (U-Th-Sm)/He ages in contrast become successively younger northward, or toward the basal UMM thrust. For the southernmost sample E05, AFT and (U-Th-Sm)/He ages are very similar, indicating rapid cooling at circa 10 Ma. Farther north, the rapid cooling signal disappears. In samples E10 to E40, the (U-Th-Sm)/He ages become successively younger while the central AFT ages remain constant, resulting in a systematic divergence between (U-Th-Sm)/He and AFT data in TS2.

[54] Across the basal UMM thrust (Figure 4) we observe a distinct increase in (U-Th-Sm)/He ages and a change from strongly to weakly annealed AFT ages. Within TS-3, the AFT ages and the number of grain age populations decrease northward, while the (U-Th-Sm)/He ages remain constant. At the northern tip of the triangle zone (TS-3), both thermochronometers yield an age of circa 8 Ma.

[55] North of the triangle zone (TS-4), the (U-Th-Sm)/He ages record significant post-depositional cooling, while the AFT ages are only partially annealed. A distinct increase in AFT ages is observed between TS-3 and TS-4, whereas the mean (U-Th-Sm)/He ages are similar. Farther north, the mean (U-Th-Sm)/He ages increase again and become older than their corresponding stratigraphic age. Ages of the two thermochronometers overlap, indicating rapid exhumation prior to deposition.

[56] At Rigi, a different pattern emerges (Figure 5). For the southernmost sample (RH05), AFT and (U-Th-Sm)/He ages differ strongly. Hence, the rapid cooling at 10 Ma found in the southernmost Entlebuch area is not discernible in the Rigi area. In the latter, the AFT ages are successively younger in TS-1 and TS-2 toward the north, but the corresponding (U-Th-Sm)/He ages are uniform or increase slightly. At the northern end of TS-2 along both sections, the ages of both thermochronometers overlap within error.

[57] North of the basal UMM thrust, we find a clear offset in both AFT and (U-Th-Sm)/He ages, which is in line with the findings from the Entlebuch. In TS-3, most of the ages are still younger than or equal to the stratigraphic age, indicating that they cooled from temperatures within the partial annealing and partial retention zone after deposition.

[58] In TS-4 along the Rigi section, AFT ages scatter substantially, while the (U-Th-Sm)/He ages decrease northward. For sample RH60, the (U-Th-Sm)/He and AFT ages are inverted. This phenomenon is also known from other studies and usually attributed to annealing kinetics and

radiation damage [*Flowers et al.*, 2009]. However, this holds only true for slowly cooled samples, or samples with high effective uranium contents [*Valla et al.*, 2012], which is not the case in our study. The AFT age is based on six single grain ages only and is therefore not considered very reliable.

[59] In TS-4, the AFT ages are older, while the (U-Th-Sm)/He ages are younger than the stratigraphic ages. A weak trend toward successively younger (U-Th-Sm)/He ages toward the north coincides with a decreasing gap between stratigraphic and these ages (Figure 5).

4.4. Thermal Modeling of the Data

[60] We constrained thermal histories from forward and inverse modeling of the AFT and (U-Th-Sm)/He data with the HeFTy v1.7.0 software [*Ketcham*, 2005]. Where available, models are based on single-grain fission track (including one to four Dpar measurements per counted grain) and single grain (U-Th-Sm)/He data. For the (U-Th-Sm)/He ages, we added a 10% error to the analytical error to account for inaccurate α ejection corrections. Inverse models were run until 100 statistically good paths (goodness of fit >0.5) were achieved. If this was not possible, at least 10,000 independent t-T paths were calculated.

[61] For modeling the kinetic properties of the apatites used for (U-Th-Sm)/He dating, we apply the calibration of *Flowers et al.* [2009]. Stopping distances for α particles were calculated following *Ketcham* [2009] and we used the redistribution option for α calculation, accounting for potentially zoned grains. Age α correction was performed following *Ketcham* [2009]. We applied the annealing model of *Ketcham et al.* [2007a] for assessing the model parameters for the fission track ages and the *Ketcham et al.* [2007b] approach for the projection of the c axis. We did not make any assumptions about the predepositional part of the cooling history. Likewise, no constraints were set for the cooling history in the basin. For burial histories, we used published sedimentation rates and thrust loading rates as maximum values, where available [*Caron et al.*, 1989; *Sinclair*, 1997a; *Kempf et al.*, 1999].

[62] We set the end of the t-T path to present-day annual average temperatures, which were obtained from *ETHZ Institut für Kartografie und Geoinformation* [2004]. We took temperature at the time of deposition from *Mosbrugger et al.* [2005]. We allow for rapid exhumation of the hinterland at any time before reburial. For the basin history, we assumed temperatures not higher than 140°C at any time after burial. This temperature is significantly higher than that required for resetting of the systems used in this study. Accordingly, neither the hinterland cooling nor the basin time-temperature history was constrained.

[63] By using both inverse and forward modeling, we tested (1) preliminary interpretations of the data set (i.e., the presence and magnitude of a 10 Ma cooling event), (2) the potential presence and magnitude of rapid cooling at 5 Ma, as discussed in literature [*Cederbom et al.*, 2004, 2011] and (3) the maximum amount of cooling which can be attributed to glacial or postglacial erosion (i.e., 2 Ma or later). We estimated the maximum and minimum amounts of cooling for each event using 1-D forward modeling. Furthermore, we tested whether the samples may have cooled at a constant rate after reburial.

4.5. Modeled Burial and Exhumation Histories

[64] Figure 7 shows the modeling results. Modeling shows that all samples in TS-1 and TS-2 have undergone total or nearly total resetting of the AFT system, as visible by the unconstrained predepositional time-temperature histories. Postdepositional heating still affected all samples in TS-3. In the Entlebuch, samples in TS-3 must have reached temperatures of at least 110°C. In the Rigi area, heating to ~90°C still produces good fits with the data. In TS-4, the influence of the source areas is significant, and the ages are eventually detrital, meaning that they have not been reheated above ~40°C after deposition. Despite similarities between the Rigi and the Entlebuch cross sections, differences in their exhumation histories are also discernible.

[65] In TS-1 of the Entlebuch profile, the sediments were heated to temperatures of at least 110°C after deposition. A strong exhumation signal at circa 10 Ma is required, which cools the sample to at least 40°C. At lower temperatures, the range of possible t-T paths becomes variable. Accordingly, the cooling from 40°C to present-day temperatures may have taken place at any point in time between 10 and 0 Ma, and is beyond thermochronological resolution. Modeling also shows that the thermochronological data cannot be explained by constant cooling after the samples reached their maximum temperatures within the basin.

[66] In the southern part of TS-2 (sample E10), a rapid cooling pulse at circa 8 Ma can be observed, thus postdating the cooling event in TS-1. This signal must account for at least 70°C of cooling. Crossing a local thrust within the tectonic slice, less rapid cooling starting at circa 10 Ma is observed (sample E20), which also must account for 60–70°C of cooling. At the northern tip of TS-2 (sample E40), a rapid cooling signal of at least ~60°C at circa 6 Ma is required to explain the obtained thermochronology ages.

[67] In TS-3 (E45), models predict rapid cooling between 12 and 10 Ma, i.e., at the same time as TS-1 and earlier than TS-2. This illustrates that no uniform trend in cooling from south to north is present. Moreover, this late Miocene pulse must account for at least ~70°C of cooling. After circa 7 Ma, modeling solutions show a wider spread, allowing for either constant exhumation since then, or short cooling pulses. At the northern end of TS-3, AFT and (U-Th-Sm)/He ages are identical within error (E50). Modeling corroborates a strong cooling signal at circa 8 Ma, coeval to cooling in TS-2. However, the models do only provide acceptable fits for the data (Figure 7).

[68] In TS-4, an increasing hinterland influence (i.e., the predeposition exhumation history) on the samples is indicated by the modeling. The samples close to TS-3 (E55 and E60) experienced postdepositional heating, but were not completely reset. Accordingly, in this area the fossil partial annealing–partial retention zone is exposed at the surface. Farther north in the basin (samples E65 and E70), no significant reheating occurred. Instead, a strong hinterland signal becomes visible, showing rapid exhumation of the source area at circa 20 Ma. This is in line with previous studies investigating the exhumation of the central Alps [e.g., *Bernet et al.*, 2009; *Glotzbach et al.*, 2010].

[69] In the Rigi area, the rocks of TS-1 experienced temperatures in excess of partial annealing–partial retention zone temperatures (sample RH05). Subsequent cooling,

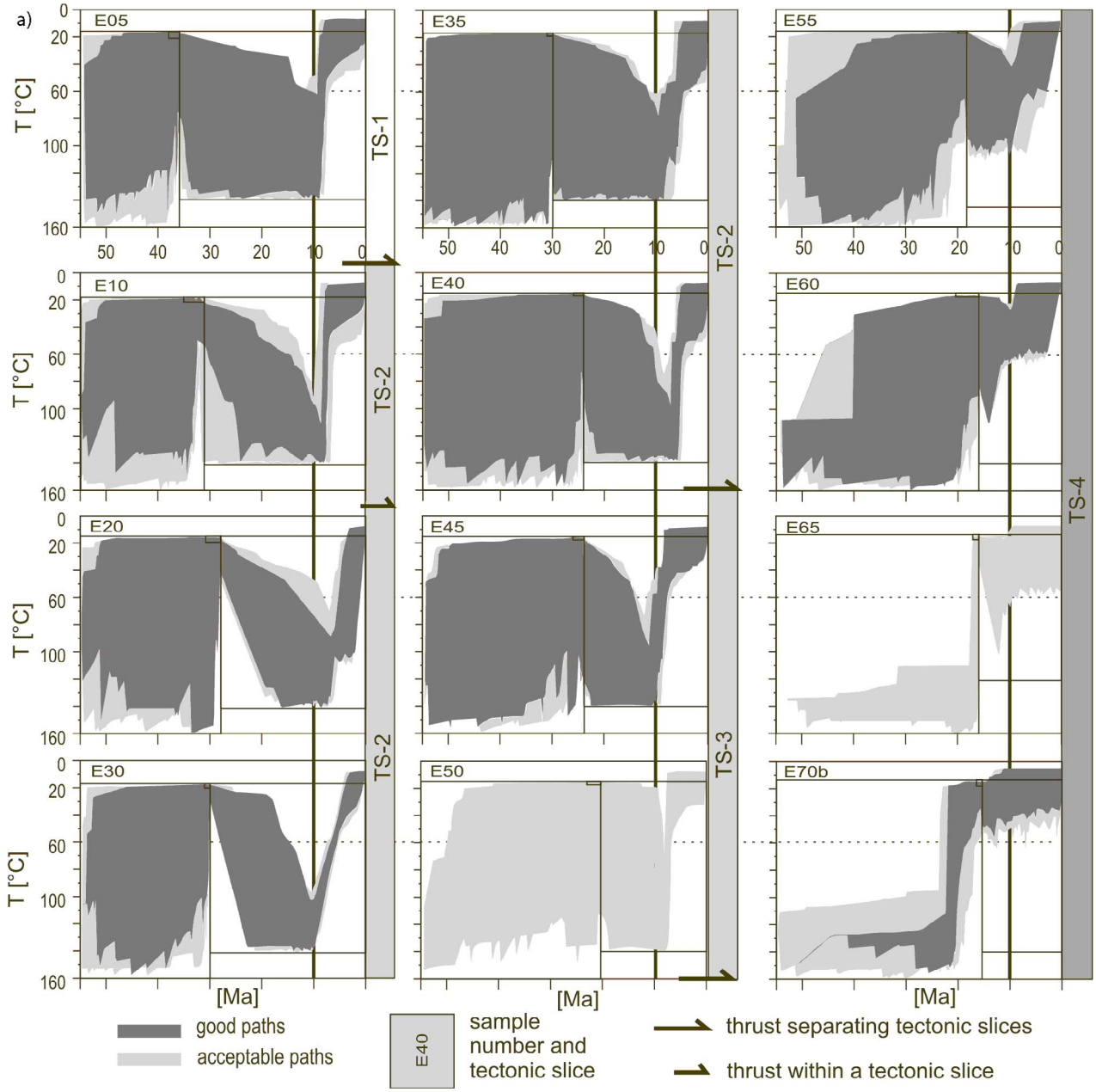

Figure 7. HeFTy modeling results for all samples discussed in the text: (a) Entlebuch samples and (b) Rigi samples. Tectonic slices are indicated by shading bars to the right of the modeling diagrams. Large thrust signs mark tectonic slice boundaries; small thrust signs denote local thrusts. Dark gray represents good fits (GOF > 0.5); light gray represents acceptable fits (GOF > 0.05) to the data. Boxes indicate predepositional time-temperature histories, constraints on depositional time and temperature and postdepositional time-temperature histories, respectively. Different exhumation pulses are visible within different samples but cluster around cooling episodes at circa 10, circa 8 and circa 6–5 Ma. No general trend from north to south is observed. Note that for samples which experienced substantial or complete resetting within the basin, the predepositional time-temperature history is unconstrained. See text for detailed discussion.

however, differs from the observations made for the southernmost Entlebuch area. A cooling pulse at circa 10 Ma may have occurred, but cannot account for the entire cooling from temperatures of at least 110°C. Instead, two alternative cooling scenarios are consistent with the observed ages at surface: (1) additional rapid cooling at circa 7 Ma and/or after 2 Ma or (2) more or less constant cooling since 10 Ma at a rate of ~10°C/Myr.

[70] In TS-2, (U-Th-Sm)/He and AFT ages are measured on different samples. Accordingly, the models are less well

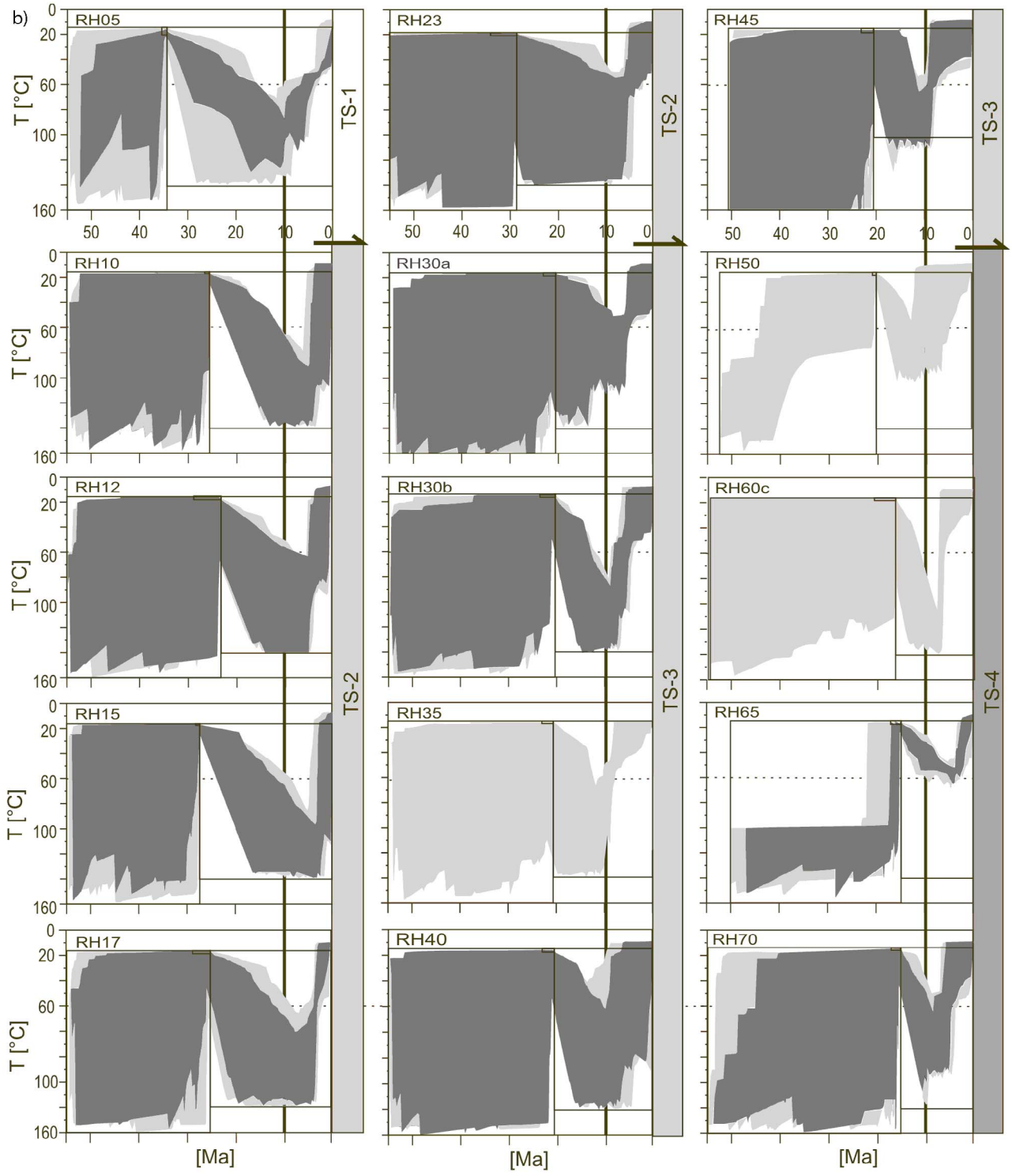

Figure 7. (continued)

constrained. All samples have undergone total annealing/resetting after deposition, and cooling started after 10 Ma (samples RH10, RH12, RH15, RH17, RH23). In addition, all samples allow for cooling starting after 5 Ma.

[71] In TS-3 (samples RH30a–RH40), all samples indicate cooling starting at circa 10 Ma. The southernmost samples (RH30a and RH30b), however, also allow for rapid cooling shortly thereafter. Generally, cooling of TS-3 occurred earlier than the rapid cooling in northernmost TS-2.

[72] In TS-4 (RH50–RH70), the samples experienced minor (<40°C) postdepositional heating, affecting mostly the (U-Th-Sm)/He system. As in the Entlebuch area, the hinterland signals are increasingly important with distance from the triangle zone. Accordingly, the fossil partial

annealing–partial retention zone is exposed at surface in the same structural position as in the Entlebuch section.

[73] In summary, modeling corroborates the observations derived from first-order data inspection, which is rapid cooling in distinct time windows. The data require rapid cooling at circa 10 Ma, circa 8 Ma, circa 6–5 Ma, and all samples allow for potential cooling after 2 Ma, in the different tectonic slices. Forward models show that this cooling signal cannot exceed a temperature difference of ~40°C and is at the limits of resolution of low-temperature thermochronology.

[74] In addition, modeling shows that the two sections have undergone similar cooling histories, with minor differences. Both sections show strong reheating in the southern part of the basin and age offsets across identical thrusts (Figures 3, 4 and 5). Differences in cooling histories between the sections are most pronounced for the southernmost samples. Finally, timing of these observed cooling signals within the different TS does not show any propagation direction along the profile (for instance getting younger toward north or south).

4.6. Comparison of External Detector Method and Laser Ablation-AFT Results

[75] In addition to gaining insights on the late history of the Alps, the data set provides the opportunity to compare the two different dating methods performed by different analysts. At Entlebuch, a sample pair suitable for comparing the two dating methods lies in the southern part of the section (E10 and MRP 179), within the southernmost units of the Subalpine Molasse (Figure 3b and Tables 1 and 2). Both samples have undergone strong to total annealing. For sample MRP 179, track length measurements show complete resetting of the sample. The obtained AFT ages are 12.3 ± 2.3 Ma and 9.8 ± 1.4 Ma for laser ablation and external detector method dating, respectively, thus reproducing within error.

[76] Sample pair E55 and MRP 198 was collected in the tilted part of the Plateau Molasse, within the USM units (Figure 3b and Tables 1 and 2). Sample E55 was collected 15 km west of sample MRP 198. The central AFT ages are 24.4 ± 3.3 Ma and 26.9 ± 1.2 Ma, and again overlap within uncertainty.

[77] Within the two sections on both flanks of the Rigi Mountain (Figures 3d and 6), the fossil partial annealing zone is evident. Even though the ages reproduce mostly within 1σ error, a slight trend toward younger ages may be inferred for the laser ablation data set.

[78] The fact that all samples are from sediments with various provenance histories and that they are located within a partial annealing zone where large single grain age variations are normal, might account for the slight differences. However, if interpreted as systematic variation, this would imply that the base of the partial annealing zone is few hundred meters higher at the western Rigi Mountain flank than at its eastern flank. Such an along-strike variation within one tectonic slice indicates variations in heat flow or differences in glacial erosion. We explore these effects for the entire data set further in the discussion (sections 5.1 and 5.2) and focus here only on the Rigi Mountain.

[79] Data density of heat flow is too poor to carry out quantitative studies, but from the Bavarian Subalpine Molasse and from the Swiss Plateau Molasse, variations in temperature gradient along strike of ~1°C/km are not exceptional [e.g., *Schärli and Rybach*, 2002]. Taking the 4 km distance between the eastern and western flank of Rigi, this results in a respective temperature difference of ~4°C. Using the present-day geothermal gradient of 30°C [*Schegg and Leu*, 1998], an offset of ~130 m in the partial annealing zone is possible.

[80] Differences in glacial erosion on the eastern and western flank of Rigi Mountain may also play a role. The surface gradient of the glacier was lower on the western side of the Rigi Mountain during the Last Glacial Maximum [*Bini et al.*, 2009], presumably resulting in slower ice velocities. However, both sides have been covered with several hundred meter thick ice sheets and present-day morphology suggests that the glacial erosion efficiency was similar on both mountain flanks [*Bini et al.*, 2009].

5. Discussion

[81] The offsets in thermochronological ages at thrusts point to a structural control of the observed age pattern. However, before automatically refer cooling to tectonic activity, we have to discuss potential influences by (1) late glacial erosion and (2) potential variations in heat or fluid flow, which could sufficiently perturb the thermal field and which might offer an alternative explanation for the observed signal.

5.1. Glacial Erosion in the North Alpine Foreland Basin

[82] Glacial activity is an important factor for the Quaternary evolution of the central Alps and the Molasse basin [e.g., *Norton et al.*, 2010; *Valla et al.*, 2011]. The modern valleys are over-deepened, witnessing the dramatic overprinting of the foreland morphology by glaciers [*Schlüchter*, 1986; *Preusser et al.*, 2010]. In the Aare valley (west of Entlebuch), incision rate possibly increased by a factor of 10 after the onset of local glaciation [*Haeuselmann et al.*, 2007]. The Aare glacier is comparable to the glaciation at Rigi in terms of ice thickness and surface gradient [*Bini et al.*, 2009]. The Entlebuch area was less affected by glaciers [*Bini et al.*, 2009]. Glacial overprinting, in turn, resulted in rapid fluvial erosion [*Schlunegger and Hinderer*, 2003; *van der Beek and Bourbon*, 2008]. This led to reshaping of the oversteepened landscape with acceleration of rock uplift in these areas and overall, more mass was removed [*Norton et al.*, 2010]. Similarly, *Champagnac et al.* [2009] concluded that the Pleistocene to present sediment production, transport and storage strongly depends on the glacial inheritance of the landscape, resulting in different erosion rates in the glaciated and nonglaciated areas. However, due to the drop in base level in the Holocene, the Entlebuch is currently undergoing incision, and is thus affected by increased postglacial processes [*Van den Berg et al.*, 2012]. In any case, the post-2 Ma cooling signal in the Alps may be related to glacial erosion [*Valla et al.*, 2011] and possibly large volumes of sediment have been removed since the Pleistocene, in particular, after 0.8–1.0 Ma [*Haeuselmann et al.*, 2007].

[83] For every sample, we evaluated the maximum amount of cooling which may have occurred within the last 2 Ma, using forward modeling with the HeFTy software. As a result it is possible to explain ~40°C of cooling by glacial

erosion in areas affected most strongly by glaciation. This is a maximum value, as we allow for zero lag times of the orogen. Using the present-day geothermal gradient, this corresponds to a potential 1–1.5 km valley deepening by glaciers that *Valla et al.* [2011] found for the Rhone valley. Results show that glacial erosion was not able to explain cooling of the samples entirely.

5.2. Heat and Fluid Flow in the North Alpine Foreland Basin

[84] Heat flow variations may influence the cooling signal of a sample, and result in an incorrect translation into erosion or tectonic activity [e.g., *Braun et al.*, 2006]. Fluid flow along thrusts may as well be responsible for locally restricted cooling of the adjacent rocks, independent of thrust activity. Therefore, a careful assessment of the origin of a thermal regime and the expected patterns is necessary to discern between different scenarios.

[85] To calculate present-day conductive heat flow densities, the corrected geothermal gradient is multiplied with the rocks' thermal conductivity [*Rybach and Bodmer*, 1983]. The latter may show variability, leading to uncertainties of up to 20% for heat flow values. However, data density in the North Alpine Foreland Basin is sufficient, and present-day geothermal gradients are known from various wells in the Molasse Basin [*Rybach and Bodmer*, 1980; *Rybach*, 1984; *Schegg and Leu*, 1998; *Schärli and Rybach*, 2002]. Based on these, a map for present-day heat flow in the Plateau Molasse is available [*Nagra*, 2002]. Generally, the heat flow decreases gradually from north to south within the flat-lying part of the Molasse basin [*Schärli and Rybach*, 2002]. For the Subalpine Molasse, data density is too low to construct reliable heat flow density maps.

[86] A study of the present-day geothermal regime of the Molasse Basin along a traverse Basel-Lucerne revealed a notable linear increase of temperature with depth in all investigated deep drillings below 400 m [*Rybach and Bodmer*, 1980]. The authors conclude that below 400 m depth, hydrologic effects that change the temperature gradient can be excluded. Accordingly, the present-day Molasse basin is in most parts dominated by conductive heat transfer, as corroborated by thermal gradients measured in boreholes and several hot springs [*Deichmann and Rybach*, 1989].

[87] Only along very limited zones, advective heat transfer is probable, which is expressed by anomalies in the heat flow pattern, possibly related to faults confining the underlying Permo-Carboniferous troughs [*Vedova et al.*, 1995; *Nagra*, 2002]. Such phenomena are restricted to distal parts of the basin and do not appear to influence the geothermal regime of the Subalpine Molasse.

[88] The paleogeothermal gradient at the time of sedimentary deposition is not commonly recoverable, and it is not likely to have remained constant throughout denudation [*Redfield*, 2010]. Vitrinite reflectance data provide an independent proxy for paleoheat flow. A comprehensive discussion on the paleogeothermal gradient and its uncertainties based on published and unpublished vitrinite reflectance data is given by *Mazurek et al.* [2006] and *Cederbom et al.* [2011]. The authors conclude that the heat flow did not change significantly during the past 10 Ma in the Swiss part of the Molasse and was probably not higher than today. Accordingly, the exhumation estimates derived from thermochronometry are minimum values.

[89] In summary, available data complemented with modeling shows that neither glacial erosion nor changes in geothermal gradient would sufficiently explain the cooling signal but a tectonic influence is required.

5.3. Heat Flow Across Active Thrusts and Lag Times Between Thrust Activity and Cooling

[90] Tectonic activity will deflect the isotherms, and in case of a cooling pulse (in contrast to constant exhumation) the thermochronometer will record posttectonic isotherm relaxation and the ages will be younger than the timing of thrust movement [e.g., *ter Voorde et al.*, 2004; *Braun et al.*, 2006]. Accordingly, when interpreting the cooling signal as thrusting, we must assess this lag time.

[91] *Wittmann et al.* [2007] argued that denudation and uplift rates correlate on a Ma timescale, indicating a denudational steady state for the central Alps during the late Neogene. This implies (at least close to) zero lag times between erosion and cooling. *ter Voorde et al.* [2004] show that, in this case, the isotherms are not warped as long as heat conduction keeps pace with advection, which is the case if the Péclet number *Pe* is smaller than 1. Similar to *ter Voorde et al.* [2004], we can use Pe = ν*(L/K), where ν is the deformation rate, L is the depth to the main detachment (=5.5 km) and K is the thermal diffusivity. Adopting a specific heat capacity of 1000 J/(kg*K) for sandstones [e.g., *Vosteen and Schellschmidt*, 2003], using thermal conductivity for the Molasse of 3.0 W/(m*K) [*Schärli*, 1989] and a density of the Molasse sandstone of 2.5 g/cm^3 [*Schärli and Rybach*, 2002], results in K = $1.2*10^{-6}$ m^2/s. This is similar to values obtained for sandstones of the eastern Molasse Basin [*Vosteen et al.*, 2003]. Accordingly, for a deformation rate $\nu > 6.8$ mm/a (i.e., $\nu > 1*K/L$), the isotherms will be perturbed by thrusting. In this case, we need to consider the response time for isotherm relaxation. *ter Voorde et al.* [2004] additionally show that substantial cooling occurs at the time of thrust movement also in the absence of erosion: for a sample located at 2 km distance from a fault dipping with 30°, an initial sample depth of 3 km and a thermal gradient of 28°C/km, the cooling due to lateral heat flow through the flanks of the hanging wall topography before onset of erosion is ~35°C. The amount of this "topographic cooling" increases with decreasing distance to the fault.

[92] We can use a first-order approach for calculating the diffusive response in one dimension following *Braun et al.* [2006], using the equation $t_d = L^2/K$, where t_d is the response time. This results in a response time for isotherm relaxation of 0.5 Ma, thus much smaller than the 1σ error of all AFT ages in this study (Table 1). Hence, we can consider the onset of cooling to be simultaneous to the onset of thrusting within the precision of the here applied thermochronometry.

5.4. Thermochronology Age Pattern Across Thrusts

[93] In order to derive the tectonic signal from the complicated and partly differing age profiles in Entlebuch and Rigi, we first discuss how tectonic activity influences the AFT and (U-Th-Sm)/He age pattern observed at surface, and second investigate whether we can trace this pattern in our data set. Figure 8 illustrates the expected thermochronological ages at surface, if an emergent thrust (i.e., a fault reaching the surface)

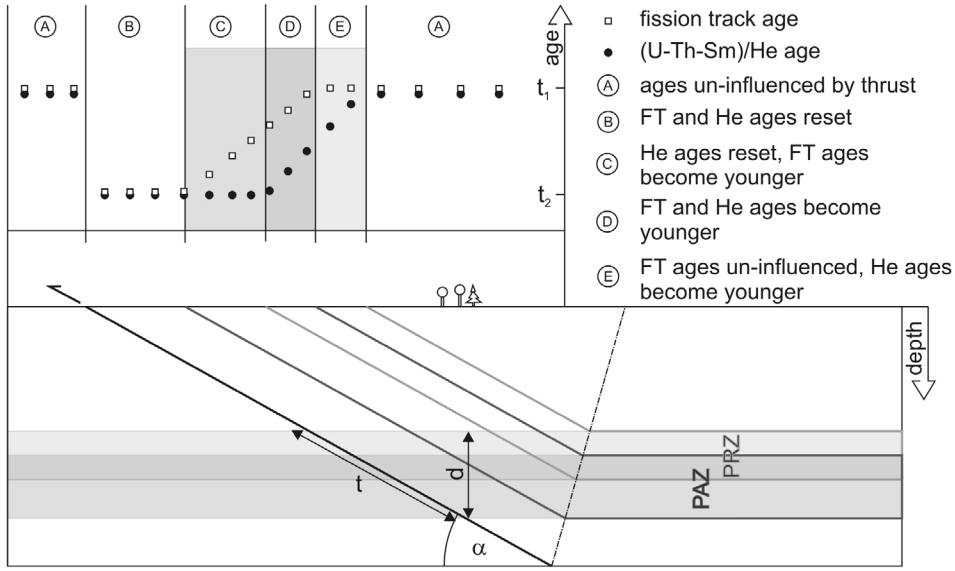

Figure 8. Conceptual sketch of the age evolution in a sample profile across a moving thrust. Different age relationships between the two thermochronometers are derived, depending on the distance to the fault. In segment E, the fission track ages stay uniform, but the (U-Th-Sm)/He ages become younger (as seen in TS-1 and TS-2 of the Entlebuch profile). In segment C, the (U-Th-Sm)/He ages stay uniform but the fission track ages become younger (as seen in TS-1 and TS-2 of the Rigi profile and in TS-3 of the Entlebuch profile). The parameter α denotes detachment dip, d denotes width from the base of the partial annealing zone to the top of the partial retention zone, and t denotes the throw on the thrust.

moves rapidly starting at t_1. We assume an arbitrary (but uniform) primary age pattern (segment denoted with A). We chose rapid exhumation along the entire section at t_1. Accordingly, all AFT and (U-Th-Sm)/He ages are identical and show an age of t_1. In the case of slow exhumation (i.e., with more separated (U-Th-Sm)/He and AFT ages) the expected age pattern affected by the thrust does not change. At t_2, rapid exhumation occurs along the thrust hanging walls. Samples from below the base of the partial annealing zone that have reached the surface, will show similar AFT and (U-Th-Sm)/He ages (segment B). They do not have an inherited age but will indicate the age of thrusting, i.e., t_2. Strictly speaking, the measured t_2 corresponds to a minimum age for thrust activity, i.e., the thrust was at least active until t_2, (but thrusting may have started earlier). With increasing distance from the thrust on its internal side, rocks that were lying within the partial annealing zone at t_2 will be exposed (segment C), showing partially annealed AFT ages (becoming successively older with increasing distances to the thrust), but (U-Th-Sm)/He ages identical to t_2. At distance from the thrust, rocks from within the partial retention zone are exposed and (U-Th-Sm)/He ages become progressively older than t_2 (segment D). At this point, both systems are not reset but still show evidence of postdepositional heating. Even farther away from the thrust, rocks from above the partial annealing zone but within the partial retention zone will be exhumed. Accordingly, the (U-Th-Sm)/He ages still show evidence of elevated temperatures, whereas the AFT system is already unaffected by the thrust (segment E). Eventually, both thermochronometers will only display the primary age pattern again (segment A).

[94] In summary, exhumation ages decrease with distance from an emergent thrust in the case where there are splays from a shallow dipping to subhorizontal detachment fault with a stratigraphic cutoff angle of near 0°, as is the case for the northern Alps [e.g., *Burkhard and Sommaruga*, 1998]. Note that with a simple movement along the thrust, different age relationships of the two thermochronometers are expected. In segment E, the AFT ages are uniform and the (U-Th-Sm)/He ages decrease, whereas in segment C, the (U-Th-Sm)/He ages are uniform and the AFT ages decrease. In this simple sketch, age relations in the hanging wall are only dependent on the distance from the sample to the thrust or the location of the thrust with respect to the positions of the partial annealing zone and partial retention zone. In a more complex geological setting (such as closely spaced thrusts active at the same time), temporal variations in heat flux across the thrust, others than flat lying isotherms, repeated movements along the thrust or irregular thrust geometry may further influence the age pattern.

[95] These thermal effects and the consequences for the correct interpretation of cooling ages has been the focus of previous studies [e.g., *Stüwe et al.*, 1994; *Moore and England*, 2001; *Braun*, 2002; *Husson and Moretti*, 2002; *Ehlers and Farley*, 2003; *Ehlers*, 2005; *Braun et al.*, 2006]. 2D and 3D numerical models can predict the age patterns along a moving thrust by solving the heat equation [e.g., *Ehlers et al.*, 2003; *Braun et al.*, 2006; *Lock and Willett*, 2008; *Robert et al.*, 2009; *Campani et al.*, 2010; *Herman et al.*, 2010]. Warping of the isotherms and the accordingly varying thermochronological ages depend on décollement depth, fault dip and fault slip rate. Minimum ages occur next to the emerging fault ramp and ages increase above the flats. *Lock and Willett* [2008] predict abrupt changes in thermochronological ages across emergent reactivated thrusts, as observed for the Subalpine Molasse. Accordingly, numerical

models (Figure 7) fit well with the qualitative reasoning and predictions.

5.5. Tectonic Evolution of the Subalpine Molasse

[96] Both first-order data inspection and subsequent modeling show that discrete cooling pulses at circa 10, 8, and 6–5 Ma can be derived from the data set. An apparent discrepancy within age trends is discovered: the (U-Th-Sm)/He ages remain constant while the AFT ages show a trend toward younger ages in some parts and a trend toward older ages in other regions.

[97] In the Entlebuch, TS-1 and TS-2 display a pattern that is similar to segment E in Figure 8. Modeling shows rapid exhumation at different periods for different samples. Accordingly, tectonic activity at a thrust between TS-1 and TS-2 and at the thrust just north of E10 is suggested at circa 10 and circa 8 Ma, respectively. The offset between TS-2 and TS-3, which is the basal USM thrust, is evident from the (U-Th-Sm)/He ages, the single grain AFT ages as well as from modeling. Thrusting must have been active until at least circa 6–5 Ma. TS-3 shows a thermochronological age pattern similar to the segments C in Figure 8. Supported by large offsets in the data set between TS-3 and TS-4, the topmost structure of the triangle zone was tectonically active until at least circa 8 Ma.

[98] In the Rigi section, the interpretation of the age patterns is complicated by the fact that not all samples have both, (U-Th-Sm)/He as well as AFT data. The age patterns of TS-1 and TS-2 are similar to the segments C of Figure 8, showing rotation along the basal UMM thrust, which is in line with the findings for Entlebuch. North of the basal UMM thrust, AFT data do not show a clear trend, but within the (U-Th-Sm)/He data of TS-4, a trend toward younger ages exists. (Re)activation of a thrust within the triangle zone and consequent back thrusting of the Plateau Molasse over the underlying duplex is able to explain this trend. This implies thrusting between TS-3 and TS-4, as observed at Entlebuch. The movement must have taken place at circa 8 Ma (and could have continued thereafter).

[99] In summary, data and modeling resolve thrust activity within both profiles along the same thrusts at the same time and additional local faulting at Entlebuch. The corresponding age/elevation profiles corroborate these findings: *Cederbom et al.* [2004, 2011] observe thrusting between the Weggis and the Entlebuch well (i.e., between TS-2 and TS-3, along the basal UMM thrust). In addition, they find an offset within the vertical sections of both boreholes, which is supported by our (U-Th-Sm)/He data in the Entlebuch well (Figure 6). This offset may have occurred at any time after the exhumation of the fossil partial annealing zone and partial retention zone (i.e., after 6–5 Ma).

5.6. Calculation of Thrust Displacement and Shortening Based on Thermochronology

[100] Having observed the late Neogene reactivation of the thrusts, we can try to assess the associated amount of thrust displacement. Fault activity causes cooling of the samples from the base of the partial annealing zone to temperatures of <40°C. Knowing the dip angle of the fault (α), estimating the width of the partial annealing–partial retention zone (d) and assuming a (paleo)geothermal gradient, we can calculate the amount of thrust displacement (t) associated with the cooling pulse (Figure 8).

[101] The dip of the main Rigi thrust is 27° [*Hantke*, 2006]; the slightly steeper dip angles at Entlebuch of ~30° reduce shortening estimates. The temperature of resetting the AFT system (i.e., the depth of the base of the partial annealing zone) may vary depending on annealing kinetics. The best proxy for this is the Dpar value. The standard Durango has a Dpar value of 2.2 μm and anneals completely at ~110°C (dependent on cooling velocity) [*Carlson et al.*, 1999]. *Fitzgerald et al.* [2006] use a temperature of complete annealing of ~100°C because they observe small Dpar values ranging between 1.3 and 1.6 μm. *Cederbom et al.* [2011] assume a respective temperature of 110 ± 5°C for Dpar values between 1.5 and 1.8 μm. Despite some exceptions, all apatites in this study have a Dpar value of 1.7 or lower. Accordingly, we assume the temperature of the base of the partial annealing zone to be 105°C. However, this temperature has only little effect on the shortening estimates and yields a width of the partial annealing–partial retention zone of 65°C. Using the (paleo)geothermal gradient after *Schegg and Leu* [1998] (30°C/km for Rigi and 28°C/km for Entlebuch), this translates into a width (d) of 2.2 and 2.3 km, respectively. As $t = d/\sin \alpha$, the corresponding thrust displacement for one cooling event is 4.6 km for Entlebuch and 4.8 km for Rigi. For the three detected cooling pulses derived from the data, this sums up to a total of ~14 km of late Miocene thrust displacement within the Subalpine Molasse, which is distributed over different thrusts. The corresponding late Miocene horizontal shortening within the Subalpine Molasse ($s = d/\tan \alpha$) is ~12 km. Additional Holocene tectonic activity of the Subalpine Molasse is beyond the resolution of the applied thermochronometers.

5.7. The Link to the Inner Alps and the Jura Mountains

[102] The thrusts of the Subalpine Molasse connect to the Alpine sole thrust and hence to the base of the Aar Massif [*Boyer and Elliott*, 1982; *Burkhard*, 1990; *Pfiffner et al.*, 1990; *Burkhard and Sommaruga*, 1998]. Similarly, the basal Jura thrust is rooted beneath the Aar Massif [*Boyer and Elliott*, 1982; *Laubscher*, 1986; *Burkhard*, 1990; *Escher and Beaumont*, 1997; *Burkhard and Sommaruga*, 1998]. Figure 9 shows the tectonic relationship of the Subalpine Molasse to the orogen. The exhumation of the Aar and Gotthard Massifs are constrained by several recent studies [*Michalski and Soom*, 1990; *Reinecker et al.*, 2008; *Vernon et al.*, 2009; *Glotzbach et al.*, 2010, 2011; *Valla et al.*, 2012; *Weisenberger et al.*, 2012]. Finally, the thrusting pulses detected in the Subalpine Molasse are synchronous with exhumation of related structures within the orogen and correspond reasonably well with the exhumation events detected by *Vernon et al.* [2009] and the 10 Ma exhumation signal argued for by *Valla et al.* [2012].

[103] Most of the exhumation and displacement of the Aar Massif (since 10 Ma) is related to displacement within the Subalpine Molasse and the Jura Mountains because of this kinematic linkage via common detachments [*Boyer and Elliott*, 1982; *Burkhard*, 1990; *Escher and Beaumont*, 1997; *Pfiffner et al.*, 1997a, 1997b]. Contemporaneous shortening in the Jura is ~5–7 km [*Burkhard*, 1990; *Philippe et al.*, 1996]. This is a bulk measurement across a subhorizontal detachment and thus requires that thrust displacement is approximately the same. We can therefore estimate ~20 km

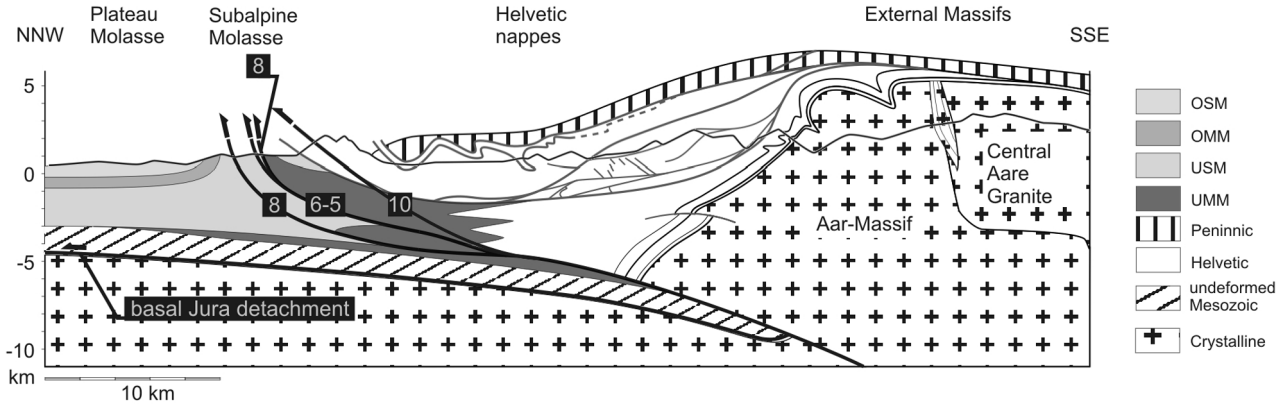

Figure 9. Tectonic link of the fault planes from the inner Alps to the Subalpine Molasse. The profile is based on the work by *Pfiffner* [2010] and is located between the Rigi and Entlebuch profiles. Active structures within the Subalpine Molasse are marked with thick black lines. Numbers in black boxes indicate the derived time of thrust activity (in Ma). Note that the southernmost active thrust must be linked to the Alpine sole thrust, as the basal Helvetic thrust is deformed by later up doming of the Aar Massif.

of displacement of the frontal Aar Massif since 10 Ma. This value fits to estimates by *Burkhard* [1990], who calculates at least 30 km of northward displacement of the frontal Aar Massif to account for the entire displacement within the Jura Mountains and the Subalpine Molasse (possibly starting as early as Oligocene times [e.g., *Pfiffner*, 1986; *Kempf et al.*, 1999]).

5.8. What Drives Exhumation in the Molasse?

[104] Figure 10 shows a compilation of periods of exhumation reported from the External Crystalline Massifs studies [*Michalski and Soom*, 1990; *Reinecker et al.*, 2008; *Vernon et al.*, 2009; *Glotzbach et al.*, 2010, 2011; *Valla et al.*, 2012; *Weisenberger et al.*, 2012], the Subalpine Molasse [this study, *Cederbom et al.*, 2004, 2011], the Plateau Molasse [*Mazurek et al.*, 2006; *Cederbom et al.*, 2011] and the Jura Mountains [*Laubscher*, 1986; *Burkhard*, 1990; *Laubscher*, 1992; *Bollinger et al.*, 1993; *Philippe et al.*, 1996; *Burkhard and Sommaruga*, 1998; *Ustaszewski et al.*, 2005; *Ustaszewski and Schmid*, 2006; *Madritsch et al.*, 2009, 2010]. Dark gray boxes denote documented periods of exhumation, light gray boxes denote periods where exhumation is plausible but the exact timing is not well constrained.

[105] Thrusting within the Subalpine Molasse is contemporaneous with, and linked to folding of the Jura Mountains and occurs when the Adriatic and European Plates are actively converging [e.g., *Mazzoli and Helman*, 1994]. Furthermore, the late Neogene thrusting pulses are not (all) correlated with climatic changes within the North Alpine Foreland Basin [*Mosbrugger et al.*, 2005]. As the response time of the system is short (circa 0.5 Ma), a climatic trigger for the detected thrusting pulses seems unlikely. Accordingly, we relate the thrusting and contemporaneous erosion which we can discern from our data to plate tectonics. For the southern part of the Subalpine Molasse, we can estimate

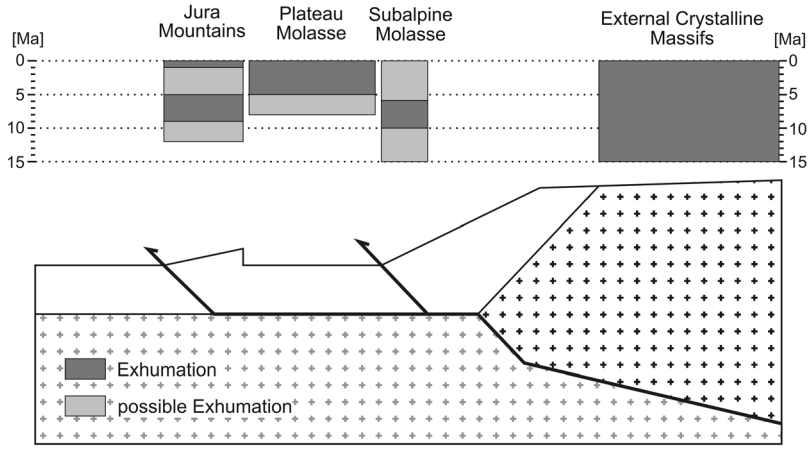

Figure 10. Correlation of different events within the Jura, the Subalpine Molasse and the External Massifs (gray boxes). It is still debated whether the exhumation of the External Massifs was continuous or accelerated in certain time windows (see text for discussion of the different hypothesis). In any case, the exhumation is contemporaneous with thrusting in the Jura Mountains and the Subalpine Molasse. Whether additional thrusting occurred within the Subalpine Molasse due to Quaternary erosion is beyond the resolution of the applied thermochronometers.

a minimum of 3.5 km of eroded section, using present-day geotherm and the base of the partial annealing zone at 105°C. The contribution to exhumation of 2.2 and 2.3 km for the Rigi and Entlebuch respectively, means that ~60% of the reported erosion signal within the Subalpine Molasse has tectonic causes. This may be seen as a synchronous adjustment across numerous structures during maintenance of a critical tapered orogen, as also seen in other case studies [e.g., *Zhang et al.*, 2004; *Simoes and Avouac*, 2006] and analogue models [*Lohrmann et al.*, 2003].

[106] The remaining 1.2 km of erosion (or 40°C of cooling) within the Subalpine Molasse may at least partly be explained differently. The late exhumation of the Plateau Molasse requires an additional process, as the underlying detachment is subhorizontal. *Cederbom et al.* [2004; 2011] argue for climate-induced postorogenic isostatic rebound as primary driving mechanism. *Schlunegger and Mosar* [2011] conclude that climate did not imprint the Alpine landscape until Plio-Pleistocene times but reorganization of the drainage pattern and consequent recycling of Molasse sediments since 5 Ma may have reactivated the thrusts to maintain the critical taper of the orogen. Eventually, geodynamic processes such as mantle delamination may contribute to accelerated uplift of the Plateau and Subalpine Molasse. For a more detailed discussion, the reader is referred to *Cederbom et al.* [2011]. On the basis of our data set, the ultimate cause for the last 1.2 km of erosion remains speculative.

6. Conclusions

[107] In this study, we show that faults in the Subalpine Molasse are tectonically active at circa 10, circa 8 and circa 6–5 Ma and possibly thereafter. The individual active thrusts can be identified for every time window. We find that thrusting is propagating neither to the foreland nor hinterland. Tectonic activity can be traced back into the orogen, where the external crystalline massifs were exhumed at the same time. Thrusting is also coeval with and potentially linked to the deformation of the Jura Mountains. The data presented here bridge the gap between the so far assumed cessation of thrusting in the Subalpine Molasse at circa 10 Ma and the recently reported thrusting at circa 5 Ma. We can infer that at least 60% of the so far elusive increased erosion signal within the foreland basin of the Alps is related to tectonic forcing.

[108] **Acknowledgments.** We thank Johannes Glodny and Juliane Herwig for their support in the laboratory and assistance during mineral separation. Raymond and Margaret Donelick are sincerely thanked for intense discussions and help with fission track dating. Hugo Ortner is specially thanked for accompanying us in the field and for fruitful discussions throughout the writing process. Pieter Vermeesch is thanked for implementing mixture modeling of ICP-MS based data to RadialPlotter and for help with statistical issues. Discussions with Mark Handy, Peter van der Beek, Todd Ehlers, Roderick Brown, Ed Sobel and Jean-Philippe Avouac were helpful to clarify the picture and are greatly appreciated. Andy Carter, Pierre Valla and Hugh Sinclair are thanked for careful and constructive reviews on an earlier version of this manuscript. This research was conducted in the framework of the ESF TopoEurope CRP "Thermo-Europe." The German Research Foundation (DFG) provided funding by research grant CE 175/1-1.

References

Affolter, T., and J.-P. Gratier (2004), Map view retrodeformation of an arcuate fold-and-thrust belt: The Jura case, *J. Geophys. Res.*, *109*(B3), B03404, doi:10.1029/2002JB002270.

Allen, P. A., S. L. Crampton, and H. D. Sinclair (1991), The inception and early evolution of the North Alpine Foreland Basin, Switzerland, *Basin Res.*, *3*(3), 143–163, doi:10.1111/j.1365-2117.1991.tb00124.x.

Äppli, A. (1897), Aus der Geschichte der Erde, *Schweiz. Paedagog. Z.*, *7*(1), 30–46.

Armstrong, P. A., T. A. Ehlers, D. S. Chapman, K. A. Farley, and P. J. J. Kamp (2003), Exhumation of the central Wasatch Mountains, Utah: 1. Patterns and timing of exhumation deduced from low-temperature thermochronology data, *J. Geophys. Res.*, *108*(B3), 2172, doi:10.1029/2001JB001708.

Becker, A. (2000), The Jura Mountains—An active foreland fold-and-thrust belt?, *Tectonophysics*, *321*(4), 381–406, doi:10.1016/S0040-1951(00)00089-5.

Berge, T. B., and S. L. Veal (2005), Structure of the Alpine foreland, *Tectonics*, *24*, TC5011, doi:10.1029/2003TC001588.

Berger, J. P., B. Reichenbacher, D. Becker, M. Grimm, K. Grimm, L. Picot, A. Storni, C. Pirkenseer, and A. Schaefer (2005a), Eocene-Pliocene time scale and stratigraphy of the Upper Rhine Graben (URG) and the Swiss Molasse Basin (SMB), *Int. J. Earth Sci.*, *94*(4), 711–731, doi:10.1007/s00531-005-0479-y.

Berger, J. P., B. Reichenbacher, D. Becker, M. Grimm, K. Grimm, L. Picot, A. Storni, C. Pirkenseer, C. Derer, and A. Schaefer (2005b), Paleogeography of the Upper Rhine Graben (URG) and the Swiss Molasse Basin (SMB) from Eocene to Pliocene, *Int. J. Earth Sci.*, *94*(4), 697–710, doi:10.1007/s00531-005-0475-2.

Bernet, M., M. Brandon, J. Garver, M. L. Balestieri, B. Ventura, and M. Zattin (2009), Exhuming the Alps through time: Clues from detrital zircon fission-track thermochronology, *Basin Res.*, *21*(6), 781–798, doi:10.1111/j.1365-2117.2009.00400.x.

Bini, A., et al. (2009), *Die Schweiz während des letzteiszeitlichen Maximums*, Bundesamt für Landestopografie Swisstopo, Wabern, Switzerland.

Bollinger, T., B. Engesser, and M. Weidmann (1993), Première découverte de mammifères pliocènes dans le Jura neuchâtelois, *Eclogae Geol. Helv.*, *86*(3), 1031–1068.

Boyer, S. E., and D. Elliott (1982), Thrust systems, *AAPG Bull.*, *66*(9), 1196–1230.

Braun, J. (2002), Quantifying the effect of recent relief changes on age-elevation relationships, *Earth Planet. Sci. Lett.*, *200*(3–4), 331–343, doi:10.1016/S0012-821X(02)00638-6.

Braun, J., P. A. Van der Beek, and G. Batt (2006), *Quatitative Thermochronology: Numerical Methods for the Interpretation of Thermochronological Data*, 1st ed., 270 pp., Cambridge Univ. Press, New York, doi:10.1017/CBO9780511616433.

Burkhard, M. (1990), Aspects of large-scale Miocene deformation in the most external part of the Swiss Alps (Subalpine Molasse to Jura fold belt), *Eclogae Geol. Helv.*, *83*(3), 559–583.

Burkhard, M., and A. Sommaruga (1998), Evolution of the western Swiss Molasse basin: Structural relations with the Alps and the Jura belt, in *Faulting, Fracturing and Igneous Intrusion in the Earth's Crust*, edited by A. Mascle et al., *Geol. Soc. Spec. Publ.*, *134*, 279–298, doi:10.1144/GSL.SP.1998.134.01.13.

Cadisch, J. (1928), Das Werden der Alpen im Spiegel der Vorlandsedimentation, *Geol. Rundsch.*, *19*(2), 105–119, doi:10.1007/BF01769026.

Campani, M., N. Mancktelow, D. Seward, Y. Rolland, W. Müller, and I. Guerra (2010), Geochronological evidence for continuous exhumation through the ductile-brittle transition along a crustal-scale low-angle normal fault: Simplon Fault Zone, central Alps, *Tectonics*, *29*, TC3002, doi:10.1029/2009TC002582.

Carlson, W. D., R. A. Donelick, and R. A. Ketcham (1999), Variability of apatite fission-track annealing kinetics: I. Experimental results, *Am. Mineral.*, *84*(9), 1213–1223.

Caron, C., P. Homewood, and W. Wildi (1989), The original Swiss flysch: A reappraisal of the type deposits in the Swiss prealps, *Earth Sci. Rev.*, *26*, 1–45, doi:10.1016/0012-8252(89)90002-0.

Cederbom, C. E., H. D. Sinclair, F. Schlunegger, and M. K. Rahn (2004), Climate-induced rebound and exhumation of the European Alps, *Geology*, *32*(8), 709–712, doi:10.1130/G20491.1.

Cederbom, C. E., F. Schlunegger, P. A. van der Beek, H. D. Sinclair, and O. Oncken (2011), Rapid, extensive erosion of the North Alpine foreland basin at 5–4 Ma, *Basin Res.*, *23*(5), 528–550, doi:10.1111/j.1365-2117.2011.00501.x.

Champagnac, J. D., F. Schlunegger, K. Norton, F. von Blanckenburg, L. M. Abbuhl, and M. Schwab (2009), Erosion-driven uplift of the modern central Alps, *Tectonophysics*, *474*(1–2), 236–249, doi:10.1016/j.tecto.2009.02.024.

Deichmann, N., and L. Rybach (1989), Earthquakes and temperatures in the lower crust below the northern Alpine foreland of Switzerland, in *Properties and Processes of the Earth's Lower Crust*, *Geophys. Monogr. Ser.*, vol. 51,

edited by R. F. Mereu, S. Mueller, and D. M. Fountain, pp. 197–213, AGU, Washington, D. C., doi:10.1029/GM051p0197.

Delacou, B., C. Sue, J. D. Champagnac, and M. Burkhard (2004), Present-day geodynamics in the bend of the western and central Alps as constrained by earthquake analysis, *Geophys. J. Int.*, *158*(2), 753–774, doi:10.1111/j.1365-246X.2004.02320.x.

Ehlers, T. A. (2005), Crustal thermal processes and the interpretation of thermochronometer data, *Rev. Mineral. Geochem.*, *58*(1), 315–350, doi:10.2138/rmg.2005.58.12.

Ehlers, T. A., and K. A. Farley (2003), Apatite (U-Th)/He thermochronometry: Methods and applications to problems in tectonic and surface processes, *Earth Planet. Sci. Lett.*, *206*(1–2), 1–14, doi:10.1016/S0012-821X(02)01069-5.

Ehlers, T. A., S. D. Willett, P. A. Armstrong, and D. S. Chapman (2003), Exhumation of the central Wasatch Mountains, Utah: 2. Thermokinematic model of exhumation, erosion, and thermochronometer interpretation, *J. Geophys. Res.*, *108*(B3), 2173, doi:10.1029/2001JB001723.

Escher, A., and C. Beaumont (1997), Formation, burial and exhumation of basement nappes at crustal scale: A geometric model based on the western Swiss-Italian Alps, *J. Struct. Geol.*, *19*(7), 955–974, doi:10.1016/S0191-8141(97)00022-9.

ETHZ Institut für Kartografie und Geoinformation (2004), *Atlas der Schweiz 2.0.2*, Swisstopo, Zürich, Switzerland.

Fitzgerald, P. G., S. L. Baldwin, L. E. Webb, and P. B. O'Sullivan (2006), Interpretation of (U-Th)/He single grain ages from slowly cooled crustal terranes: A case study from the Transantarctic Mountains of southern Victoria Land, *Chem. Geol.*, *225*(1–2), 91–120, doi:10.1016/j.chemgeo.2005.09.001.

Flowers, R. M., R. A. Ketcham, D. L. Shuster, and K. A. Farley (2009), Apatite (U-Th)/He thermochronometry using a radiation damage accumulation and annealing model, *Geochim. Cosmochim. Acta*, *73*(8), 2347–2365, doi:10.1016/j.gca.2009.01.015.

Galbraith, R. F. (2005), *Statistics for Fission Track Analysis*, CRC Press, Boca Raton, Fla., doi:10.1201/9781420034929.

Ganss, O., and P. Schmidt-Thomé (1953), Die gefaltete Molasse am Alpenrand zwischen Bodensee und Salzach, *Z. Dtsch. Geol. Ges.*, *105*, 402–495.

Giamboni, M., K. Ustaszewski, S. M. Schmid, M. E. Schumacher, and A. Wetzel (2004), Plio-Pleistocene transpressional reactivation of Paleozoic and Paleogene structures in the Rhine-Bresse transform zone (northern Switzerland and eastern France), *Int. J. Earth Sci.*, *93*(2), 207–223, doi:10.1007/s00531-003-0375-2.

Glotzbach, C., J. Reinecker, M. Danišík, M. Rahn, W. Frisch, and C. Spiegel (2010), Thermal history of the central Gotthard and Aar massifs, European Alps: Evidence for steady state, long-term exhumation, *J. Geophys. Res.*, *115*, F03017, doi:10.1029/2009JF001304.

Glotzbach, C., P. A. van der Beek, and C. Spiegel (2011), Episodic exhumation and relief growth in the Mont Blanc massif, Western Alps from numerical modelling of thermochronology data, *Earth Planet. Sci. Lett.*, *304*(3–4), 417–430, doi:10.1016/j.epsl.2011.02.020.

Haeuselmann, P., D. E. Granger, P.-Y. Jeannin, and S.-E. Lauritzen (2007), Abrupt glacial valley incision at 0.8 Ma dated from cave deposits in Switzerland, *Geology*, *35*(2), 143–146, doi:10.1130/G23094A.

Hantke, R. (2006), Blatt 1151 Rigi, in *Geologie Atlas Schweiz*, scale 1:25,000, Erläut.116, Bundesamt für Landestopografie, Bern.

Heim, A. (1919), *Geologie der Schweiz*, vol. 1, Molasseland und Juragebirge, Leipzig, Germany.

Herman, F., et al. (2010), Exhumation, crustal deformation, and thermal structure of the Nepal Himalaya derived from the inversion of thermochronological and thermobarometric data and modeling of the topography, *J. Geophys. Res.*, *115*, B06407, doi:10.1029/2008JB006126.

Homewood, P. W., P. A. Allen, and G. D. Williams (1986), Dynamics of the Molasse Basin of western Switzerland, in *Foreland Basins*, edited by P. A. Allen and P. W. Homewood, pp. 199–217, Int. Assoc. of Sedimentol., Oxford, U. K., doi:10.1002/9781444303810.ch10.

Husson, L., and I. Moretti (2002), Thermal regime of fold and thrust belts—An application to the Bolivian sub Andean zone, *Tectonophysics*, *345*(1–4), 253–280, doi:10.1016/S0040-1951(01)00216-5.

Kälin, D. (1997), Litho- und Biostratigraphie der Mittel- bis Obermiozänen Bois De Raube-Formation (Nordwestschweiz), *Eclogae Geol. Helv.*, *90*, 97–114.

Kempf, O., and O. A. Pfiffner (2004), Early Tertiary evolution of the North Alpine Foreland Basin of the Swiss Alps and adjoining areas, *Basin Res.*, *16*(4), 549–567, doi:10.1111/j.1365-2117.2004.00246.x.

Kempf, O., A. Matter, D. W. Burbank, and M. Mange (1999), Depositional and structural evolution of a foreland basin margin in a magnetostratigraphic framework: The eastern Swiss Molasse, *Int. J. Earth Sci.*, *88*(2), 253–275, doi:10.1007/s005310050263.

Ketcham, R. A. (2005), Forward and inverse modeling of low-temperature thermochronometry data, *Rev. Mineral. Geochem.*, *58*(1), 275–314, doi:10.2138/rmg.2005.58.11.

Ketcham, R. A. (2009), Refinements for alpha stopping distances and FT corrections, *Ontrack*, *16*(2). [Available at http://www.ontrackforum.org/index.php?option=com_content&view=article&id=85:refinements-for-alpha-stopping-distances-and-ft-corrections&catid=24:articles&Itemid=94].

Ketcham, R. A., A. Carter, R. A. Donelick, J. Barbarand, and A. J. Hurford (2007a), Improved modeling of fission-track annealing in apatite, *Am. Mineral.*, *92*(5–6), 799–810, doi:10.2138/am.2007.2281.

Ketcham, R. A., A. Carter, R. A. Donelick, J. Barbarand, and A. J. Hurford (2007b), Improved measurement of fission-track annealing in apatite using c-axis projection, *Am. Mineral.*, *92*(5–6), 789–798, doi:10.2138/am.2007.2280.

Kuhlemann, J. (2000), Post-collisional sediment budget of circum-Alpine basins (central Europe), *Mem. Sci. Geol. Padova*, *52*(1), 1–91.

Kuhlemann, J., and O. Kempf (2002), Post-Eocene evolution of the North Alpine Foreland Basin and its response to Alpine tectonics, *Sediment. Geol.*, *152*(1–2), 45–78, doi:10.1016/S0037-0738(01)00285-8.

Laubscher, H. (1961), Die Fernschubhypothese der Jurafaltung, *Eclogae Geol. Helv.*, *54*(1), 221–282.

Laubscher, H. (1986), The eastern Jura: Relations between thin-skinned and basement tectonics, local and regional, *Geol. Rundsch.*, *75*(3), 535–553, doi:10.1007/BF01820630.

Laubscher, H. (1992), Jura kinematics and the Molasse basin, *Eclogae Geol. Helv.*, *85*(3), 653–675.

Lihou, J. C., and P. A. Allen (1996), Importance of inherited rift margin structures in the early North Alpine Foreland Basin, Switzerland, *Basin Res.*, *8*(4), 425–442, doi:10.1046/j.1365-2117.1996.00244.x.

Liniger, H. (1964), Beziehungen zwischen Pliozän und Jurafaltung in der Ajoie, *Eclogae Geol. Helv.*, *57*(1), 75–90.

Lock, J., and S. D. Willett (2008), Low-temperature thermochronometric ages in fold-and-thrust belts, *Tectonophysics*, *456*(3–4), 147–162, doi:10.1016/j.tecto.2008.03.007.

Lohrmann, J., N. Kukowski, J. Adam, and O. Oncken (2003), The impact of analogue material properties on the geometry, kinematics, and dynamics of convergent sand wedges, *J. Struct. Geol.*, *25*(10), 1691–1711, doi:10.1016/S0191-8141(03)00005-1.

Madritsch, H., S. M. Schmid, and O. Fabbri (2008), Interactions between thin- and thick-skinned tectonics at the northwestern front of the Jura fold-and-thrust belt (Eastern France), *Tectonics*, *27*, TC5005, doi:10.1029/2008TC002282.

Madritsch, H., A. Kounov, S. M. Schmid, and O. Fabbri (2009), Multiple fault reactivations within the intra-continental Rhine-Bresse Transfer Zone (La Serre Horst, eastern France), *Tectonophysics*, *471*(3–4), 297–318, doi:10.1016/j.tecto.2009.02.044.

Madritsch, H., F. Preusser, O. Fabbri, V. Bichet, F. Schlunegger, and S. M. Schmid (2010), Late Quaternary folding in the Jura Mountains: Evidence from syn-erosional deformation of fluvial meanders, *Terra Nova*, *22*(2), 147–154, doi:10.1111/j.1365-3121.2010.00928.x.

Matter, A., P. W. Homewood, C. Caron, J. Van Stuijvenberg, M. Weidmann, and W. Winkler (1980), Flysch and molasse of central and western Switzerland, in *Geology of Switzerland, A Guide Book, Part B: Geological Excursions*, edited by S. G. Kommission, pp. 261–293, Wepf, Basel, Switzerland.

Mazurek, M., A. J. Hurford, and W. Leu (2006), Unravelling the multi-stage burial history of the Swiss Molasse Basin: Integration of apatite fission track, vitrinite reflectance and biomarker isomerisation analysis, *Basin Res.*, *18*(1), 27–50, doi:10.1111/j.1365-2117.2006.00286.x.

Mazzoli, S., and M. Helman (1994), Neogene patterns of relative plate motion for Africa-Europe: Some implications for recent central Mediterranean tectonics, *Geol. Rundsch.*, *83*(2), 464–468.

Michalski, I., and M. Soom (1990), The Alpine thermo-tectonic evolution of the Aar and Gotthard massifs, central Switzerland: Fission track ages on zircon and apatite and K-Ar mica ages, *Schweiz. Mineral. Petrogr. Mitt.*, *70*(3), 373–387.

Moore, M. A., and P. C. England (2001), On the inference of denudation rates from cooling ages of minerals, *Earth Planet. Sci. Lett.*, *185*(3–4), 265–284, doi:10.1016/S0012-821X(00)00380-0.

Mosar, J. (1999), Present-day and future tectonic underplating in the western Swiss Alps: Reconciliation of basement/wrench-faulting and decollement folding of the Jura and Molasse basin in the Alpine foreland, *Earth Planet. Sci. Lett.*, *173*(3), 143–155, doi:10.1016/S0012-821X(99)00238-1.

Mosbrugger, V., T. Utescher, and D. L. Dilcher (2005), Cenozoic continental climatic evolution of central Europe, *Proc. Natl. Acad. Sci. U. S. A.*, *102*(42), 14,964–14,969, doi:10.1073/pnas.0505267102.

Müller, M., F. Nieberding, and A. Wanninger (1988), Tectonic style and pressure distribution at the northern margin of the Alps between Lake

Constance and the River Inn, *Geol. Rundsch.*, *77*(3), 787–796, doi:10.1007/BF01830185.

Nagra (2002), Projekt Opalinuston Synthese der geowissenschaftlichen Untersuchungsergebnisse, *Nagra Tech. Ber. NTB 02–03*, pp. 139–142, Munich, Germany.

Norton, K. P., L. M. Abbuhl, and F. Schlunegger (2010), Glacial conditioning as an erosional driving force in the central Alps, *Geology*, *38*(7), 655–658, doi:10.1130/G31102.1.

Persaud, M., and O. A. Pfiffner (2004), Active deformation in the eastern Swiss Alps: Post-glacial faults, seismicity and surface uplift, *Tectonophysics*, *385*(1–4), 59–84, doi:10.1016/j.tecto.2004.04.020.

Pfiffner, O. A. (1986), Evolution of the north Alpine foreland basin in the central Alps, in *Foreland Basins*, edited by P. A. Allen and P. W. Homewood, pp. 219–228, Int. Assoc. of Sedimentol., Oxford, U. K., doi:10.1002/9781444303810.ch11.

Pfiffner, O. A. (2010), *Geologie der Alpen*, 2nd ed., 360 pp., UTB GmbH, Stuttgart, Germany.

Pfiffner, O. A., W. Frei, P. Valasek, M. Stäuble, L. Levato, L. DuBois, S. M. Schmid, and S. B. Smithson (1990), Crustal shortening in the Alpine Orogen: Results from deep seismic reflection profiling in the eastern Swiss Alps, Line NFP 20-east, *Tectonics*, *9*(6), 1327–1355, doi:10.1029/TC009i006p01327.

Pfiffner, O. A., P.-F. Erard, and M. Stäuble (1997a), Two cross sections through the Swiss Molasse basin (lines E4–E6, W1, W7–W110), in *Deep Structure of the Swiss Alps: Results of NRP 20*, edited by O. A. Pfiffner et al., pp. 64–72, Birkhäuser, Basel, Switzerland.

Pfiffner, O. A., S. Sahli, and M. Stäuble (1997b), Compression and uplift of the external massifs in the Helvetic zone, in *Deep Structure of the Swiss Alps: Results of NRP 20*, edited by O. A. Pfiffner et al., pp. 139–153, Birkhäuser, Basel, Switzerland.

Pfiffner, O. A., F. Schlunegger, and S. J. H. Buiter (2002), The Swiss Alps and their peripheral foreland basin: Stratigraphic response to deep crustal processes, *Tectonics*, *21*(2), 1009, doi:10.1029/2000TC900039.

Philippe, Y., B. Colletta, E. Deville, and A. Mascle (1996), The Jura fold-and-thrust belt: A kinematic model based on map-balancing, in *Peri-Tethys Memoir 2; Structure and Prospects of Alpine Basins and Forelands*, edited by P. A. Ziegler and F. Horvath, pp. 235–261, Mus. Natl. d'Hist. Nat., Paris.

Preusser, F., J. Reitner, and C. Schlüchter (2010), Distribution, geometry, age and origin of overdeepened valleys and basins in the Alps and their foreland, *Swiss J. Geosci.*, *103*(3), 407–426, doi:10.1007/s00015-010-0044-y.

Rahn, M., and R. Selbekk (2007), Absolute dating of the youngest sediments of the Swiss Molasse basin by apatite fission track analysis, *Swiss J. Geosci.*, *100*(3), 371–381, doi:10.1007/s00015-007-1234-0.

Redfield, T. F. (2010), On apatite fission track dating and the Tertiary evolution of west Greenland topography, *J. Geol. Soc.*, *167*(2), 261–271, doi:10.1144/0016-76492009-036.

Reinecker, J., M. Danisik, C. Schmid, C. Glotzbach, M. Rahn, W. Frisch, and C. Spiegel (2008), Tectonic control on the late stage exhumation of the Aar Massif (Switzerland): Constraints from apatite fission track and (U-Th)/He data, *Tectonics*, *27*, TC6009, doi:10.1029/2007TC002247.

Robert, X., P. van der Beek, J. Braun, C. Perry, M. Dubille, and J.-L. Mugnier (2009), Assessing Quaternary reactivation of the Main Central thrust zone (central Nepal Himalaya): New thermochronologic data and numerical modeling, *Geology*, *37*(8), 731–734, doi:10.1130/G25736A.1.

Rosenberg, C. L., and A. Berger (2009), On the causes and modes of exhumation and lateral growth of the Alps, *Tectonics*, *28*, TC6001, doi:10.1029/2008TC002442.

Ruffini, R., R. Polino, E. Callegari, J. C. Hunziker, and H. R. Pfeifer (1997), Volcanic clast-rich turbidites of the Taveyanne sandstones from the Thônes syncline (Savoie, France): Records for a Tertiary postcollisional volcanism, *Schweiz. Mineral. Petrogr. Mitt.*, *77*, 161–174.

Rybach, L. (1984), The paleogeothermal conditions of the Swiss Molasse basin: Implications for hydrocarbon potential, *Rev. Inst. Fr. Pet.*, *39*(2), 143–147.

Rybach, L., and P. Bodmer (1980), Die geothermischen Verhältnisse der Schweizer Geotraverse im Abschnitt Basel-Luzern, *Eclogae Geol. Helv.*, *73*(2), 501–512.

Rybach, L., and P. Bodmer (1983), Processing and representation of heat flow density maps. Part II: Construction and contouring of heat flow density maps, *Zentralbl. Geol. Palaeontol., Teil 2*, *I*, 87–92.

Schärli, U. (1989), Geothermische Detailkartierung (1:100000) in der zentralen Nordschweiz mit besonderer Berücksichtigung petrophysikalischer Parameter, PhD thesis, 166 pp., ETH Zurich, Zurich, Switzerland.

Schärli, U., and L. Rybach (2002), Erstellung einer aktuellen Karte der Temperaturgradienten und des Wärmeflusses der Nordschweiz, internal report, Nagra, Munich, Germany.

Schegg, R. (1992), Coalification, shale diagenesis and thermal modelling in the Alpine Foreland basin: The Western Molasse basin (Switzerland/France), *Org. Geochem.*, *18*(3), 289–300, doi:10.1016/0146-6380(92)90070-E.

Schegg, R., and W. Leu (1998), Analysis of erosion events and palaeogeothermal gradients in the North Alpine Foreland Basin of Switzerland, in *Faulting, Fracturing and Igneous Intrusion in the Earth's Crust*, edited by D. Healy, R. W. H. Butler, and Z. K. Shipton, *Geol. Soc. Spec. Publ.*, *141*(1), 137–155, doi:10.1144/GSL.SP.1998.141.01.09.

Schegg, R., W. Leu, C. Cornford, and P. A. Allen (1997), New coalification profiles in the Molasse Basin of western Switzerland: Implications for the thermal and geodynamic evolution of the Alpine Foreland, *Eclogae Geol. Helv.*, *90*(1), 79–96.

Schlüchter, C. (1986), The Quaternary glaciations of Switzerland, with special reference to the Northern Alpine Foreland, *Quat. Sci. Rev.*, *5*(0), 413–419.

Schlunegger, F. (1999), Controls of surface erosion on the evolution of the Alps: Constraints from the stratigraphies of the adjacent foreland basins, *Int. J. Earth Sci.*, *88*(2), 285–304, doi:10.1007/s005310050265.

Schlunegger, F., and M. Hinderer (2003), Pleistocene/Holocene climate change, re-establishment of fluvial drainage network and increase in relief in the Swiss Alps, *Terra Nova*, *15*(2), 88–95, doi:10.1046/j.1365-3121.2003.00469.x.

Schlunegger, F., and J. Mosar (2011), The last erosional stage of the Molasse Basin and the Alps, *Int. J. Earth Sci.*, *100*(5), 1147–1162, doi:10.1007/s00531-010-0607-1.

Schlunegger, F., and G. Simpson (2002), Possible erosional control on lateral growth of the European central Alps, *Geology*, *30*(10), 907–910, doi:10.1130/0091-7613(2002)030<0907:PECOLG>2.0.CO;2.

Schlunegger, F., A. Matter, D. W. Burbank, and E. M. Klaper (1997), Magnetostratigraphic constraints on relationships between evolution of the central Swiss Molasse basin and Alpine orogenic events, *Geol. Soc. Am. Bull.*, *109*(2), 225–241, doi:10.1130/0016-7606(1997)109<0225:MCORBE>2.3.CO;2.

Schlunegger, F., D. Rieke-Zapp, and K. Ramseyer (2007), Possible environmental effects on the evolution of the Alps-Molasse Basin system, *Swiss J. Geosci.*, *100*(3), 383–405, doi:10.1007/s00015-007-1238-9.

Simoes, M., and J. P. Avouac (2006), Investigating the kinematics of mountain building in Taiwan from the spatiotemporal evolution of the foreland basin and western foothills, *J. Geophys. Res.*, *111*, B10401, doi:10.1029/2005JB004209.

Sinclair, H. D. (1997a), Tectonostratigraphic model for underfilled peripheral foreland basins: An Alpine perspective, *Geol. Soc. Am. Bull.*, *109*(3), 324–346, doi:10.1130/0016-7606(1997)109<0324:TMFUPF>2.3.CO;2.

Sinclair, H. D. (1997b), Flysch to molasse transition in peripheral foreland basins: The role of the passive margin versus slab breakoff, *Geology*, *25*(12), 1123–1126, doi:10.1130/0091-7613(1997)025<1123:FTMTIP>2.3.CO;2.

Sinclair, H. D., and P. A. Allen (1992), Vertical versus horizontal motions in the Alpine orogenic wedge: Stratigraphic response in the foreland basin, *Basin Res.*, *4*(3–4), 215–232, doi:10.1111/j.1365-2117.1992.tb00046.x.

Sinclair, H. D., B. J. Coakley, P. A. Allen, and A. B. Watts (1991), Simulation of foreland basin stratigraphy using a diffusion model of mountain belt uplift and erosion: An example from the central Alps, Switzerland, *Tectonics*, *10*(3), 599–620, doi:10.1029/90TC02507.

Sissingh, W. (1997), Tectonostratigraphy of the North Alpine Foreland Basin: Correlation of Tertiary depositional cycles and orogenic phases, *Tectonophysics*, *282*(1–4), 223–256, doi:10.1016/S0040-1951(97)00221-7.

Sommaruga, A. (1997), Geology of the central Jura and the Molasse Basin: New insight into an evaporite-based foreland fold and thrust belt, *Mem. 12*, 176 pp., Soc. des Sci. Nat. de Neuchatel, Paris.

Sommaruga, A. (1999), Décollement tectonics in the Jura foreland fold-and-thrust belt, *Mar. Pet. Geol.*, *16*(2), 111–134, doi:10.1016/S0264-8172(98)00068-3.

Spicher, A. (1980), *Tektonische Karte der Schweiz*, Bundesamt für Landestopographie, Bern, Switzerland.

Stockli, D. F. (2005), Application of low-temperature thermochronometry to extensional tectonic settings, *Rev. Mineral. Geochem.*, *58*(1), 411–448, doi:10.2138/rmg.2005.58.16.

Stüwe, K., L. White, and R. Brown (1994), The influence of eroding topography on steady-state isotherms. Application to fission track analysis, *Earth Planet. Sci. Lett.*, *124*(1–4), 63–74, doi:10.1016/0012-821X(94)00068-9.

Tagami, T., and P. B. O'Sullivan (2005), Fundamentals of fission-track thermochronology, *Rev. Mineral. Geochem.*, *58*(1), 19–47, doi:10.2138/rmg.2005.58.2.

ter Voorde, M., C. H. de Bruijne, S. A. P. L. Cloetingh, and P. A. M. Andriessen (2004), Thermal consequences of thrust faulting: Simultaneous

versus successive fault activation and exhumation, *Earth Planet. Sci. Lett.*, *223*(3–4), 395–413, doi:10.1016/j.epsl.2004.04.026.

Trümpy, R. (1980), *Geology of Switzerland: A Guide Book, Part A: An Outline of the Geology of Switzerland*, edited by S. G. Kommission, Wepf, Basel.

Ustaszewski, K., and S. M. Schmid (2006), Control of preexisting faults on geometry and kinematics in the northernmost part of the Jura fold-and-thrust belt, *Tectonics*, *25*, TC5003, doi:10.1029/2005TC001915.

Ustaszewski, K., and S. M. Schmid (2007), Latest Pliocene to recent thick-skinned tectonics at the Upper Rhine Graben–Jura Mountains junction, *Swiss J. Geosci.*, *100*(2), 293–312, doi:10.1007/s00015-007-1226-0.

Ustaszewski, K., M. E. Schumacher, S. M. Schmid, and D. Nieuwland (2005), Fault reactivation in brittle–viscous wrench systems–dynamically scaled analogue models and application to the Rhine–Bresse transfer zone, *Quat. Sci. Rev.*, *24*(3–4), 363–380, doi:10.1016/j.quascirev.2004.03.015.

Valla, P. G., D. L. Shuster, and P. A. van der Beek (2011), Significant increase in relief of the European Alps during mid-Pleistocene glaciations, *Nat. Geosci.*, *4*, 688–692, doi:10.1038/ngeo1242.

Valla, P. G., P. A. van der Beek, D. L. Shuster, J. Braun, F. Herman, L. Tassan-Got, and C. Gautheron (2012), Late Neogene exhumation and relief development of the Aar and Aiguilles Rouges massifs (Swiss Alps) from low-temperature thermochronology modeling and $^{4}He/^{3}He$ thermochronometry, *J. Geophys. Res.*, *117*, F01004, doi:10.1029/2011JF002043.

Van den Berg, F., F. Schlunegger, N. Akçar, and P. Kubik (2012), ^{10}Be-derived assessment of accelerated erosion in a glacially conditioned inner gorge, Entlebuch, central Alps of Switzerland, *Earth Surf. Processes Landforms*, *37*, 1176–1188, doi:10.1002/esp.3237.

van der Beek, P., and P. Bourbon (2008), A quantification of the glacial imprint on relief development in the French western Alps, *Geomorphology*, *97*(1–2), 52–72, doi:10.1016/j.geomorph.2007.02.038.

Vedova, B. D., F. Lucazeau, V. Pasquale, G. Pellis, and M. Verdoya (1995), Heat flow in the tectonic provinces crossed by the southern segment of the European Geotraverse, *Tectonophysics*, *244*(1–3), 57–74, doi:10.1016/0040-1951(94)00217-W.

Vermeesch, P. (2009), RadialPlotter: A Java application for fission track, luminescence and other radial plots, *Radiat. Meas.*, *44*(4), 409–410, doi:10.1016/j.radmeas.2009.05.003.

Vernon, A. J., P. A. van der Beek, H. D. Sinclair, C. Persano, J. Foeken, and F. M. Stuart (2009), Variable late Neogene exhumation of the central European Alps: Low-temperature thermochronology from the Aar Massif, Switzerland, and the Lepontine Dome, Italy, *Tectonics*, *28*, TC5004, doi:10.1029/2008TC002387.

Vollmayr, T., and A. Wendt (1987), Die Erdgasbohrung Entlebuch 1, ein Tiefenaufschluss am Alpennordrand, *Bull. Schweiz. Ver. Pet. Geol. Ing.*, *53*, 67–79.

Vosteen, H.-D., and R. Schellschmidt (2003), Influence of temperature on thermal conductivity, thermal capacity and thermal diffusivity for different types of rock, *Phys. Chem. Earth Parts A/B/C*, *28*(9–11), 499–509, doi:10.1016/S1474-7065(03)00069-X.

Vosteen, H.-D., V. Rath, C. Clauser, and B. Lammerer (2003), The thermal regime of the Eastern Alps from inversion analyses along the TRANSALP profile, *Phys. Chem. Earth Parts A/B/C*, *28*(9–11), 393–405, doi:10.1016/S1474-7065(03)00060-3.

Weisenberger, T. B., M. Rahn, R. van der Lelij, R. A. Spikings, and K. Bucher (2012), Timing of low-temperature mineral formation during exhumation and cooling in the central Alps, Switzerland, *Earth Planet. Sci. Lett.*, *327–328*(0), 1–8, doi:10.1016/j.epsl.2012.01.007.

Willett, S. D., and F. Schlunegger (2010), The last phase of deposition in the Swiss Molasse Basin: From foredeep to negative-alpha basin, *Basin Res.*, *22*(5), 623–639, doi:10.1111/j.1365-2117.2009.00435.x.

Willett, S. D., F. Schlunegger, and V. Picotti (2006), Messinian climate change and erosional destruction of the central European Alps, *Geology*, *34*(8), 613–616, doi:10.1130/G22280.1.

Wittmann, H., F. von Blanckenburg, T. Kruesmann, K. P. Norton, and P. W. Kubik (2007), Relation between rock uplift and denudation from cosmogenic nuclides in river sediment in the central Alps of Switzerland, *J. Geophys. Res.*, *112*, F04010, doi:10.1029/2006JF000729.

Wolf, R. A., K. A. Farley, and L. T. Silver (1996), Helium diffusion and low-temperature thermochronometry of apatite, *Geochim. Cosmochim. Acta*, *60*(21), 4231–4240, doi:10.1016/S0016-7037(96)00192-5.

Zhang, P.-Z., et al. (2004), Continuous deformation of the Tibetan Plateau from Global Positioning System data, *Geology*, *32*(9), 809–812, doi:10.1130/G20554.1.